NAVAL POSTGRADUATE SCHOOL

MONTEREY, CALIFORNIA

THESIS

METAMATERIAL RESONANT ABSORBERS FOR TERAHERTZ SENSING

by

Eric A. Stinson

December 2015

Thesis Advisor:	Gamani Karunasiri
Co-Advisor	Fabio Alves

Approved for public release; distribution is unlimited

THIS PAGE INTENTIONALLY LEFT BLANK

1. AGENCY USE ONLY *(Leave blank)*	2. REPORT DATE December 2015	3. REPORT TYPE AND DATES COVERED Master's thesis	
4. TITLE AND SUBTITLE METAMATERIAL RESONANT ABSORBERS FOR TERAHERTZ SENSING		5. FUNDING NUMBERS	
6. AUTHOR(S) Eric A. Stinson			
7. PERFORMING ORGANIZATION NAME(S) AND ADDRESS(ES) Naval Postgraduate School Monterey, CA 93943-5000		8. PERFORMING ORGANIZATION REPORT NUMBER	
9. SPONSORING /MONITORING AGENCY NAME(S) AND ADDRESS(ES) N/A		10. SPONSORING / MONITORING AGENCY REPORT NUMBER	
11. SUPPLEMENTARY NOTES The views expressed in this thesis are those of the author and do not reflect the official policy or position of the Department of Defense or the U.S. government. IRB Protocol number ____N/A____.			
12a. DISTRIBUTION / AVAILABILITY STATEMENT Approved for public release; distribution is unlimited		12b. DISTRIBUTION CODE	

13. ABSTRACT (maximum 200 words)

The aim of this work is to develop a metamaterial absorber that can be incorporated into a terahertz (THz) imaging system with a 4.7 THz quantum cascade laser (QCL) illumination source. Finite element (FE) simulations were utilized to design metamaterials, and a Fourier transform infrared spectrometer (FTIR) was employed to characterize the absorption spectrum of each metamaterial configuration. Process parameters for future work with the microfabrication devices have been established for the Naval Postgraduate School clean room. Analysis of experimental data provided insight in determining the refractive index of the metamaterial dielectric, SiO_x, from 3–8 THz and confirmed the Lorentzian shape for the absorption spectrum as theoretically proposed by another group. Future work will incorporate the metamaterial absorber design of this research into a more efficient, cost effective, bi-material THz sensor that can be employed in a variety of naval applications.

14. SUBJECT TERMS terahertz sensors, metamaterials, uncooled detectors			15. NUMBER OF PAGES 73
			16. PRICE CODE
17. SECURITY CLASSIFICATION OF REPORT Unclassified	18. SECURITY CLASSIFICATION OF THIS PAGE Unclassified	19. SECURITY CLASSIFICATION OF ABSTRACT Unclassified	20. LIMITATION OF ABSTRACT UU

THIS PAGE INTENTIONALLY LEFT BLANK

METAMATERIAL RESONANT ABSORBERS FOR TERAHERTZ SENSING

Eric A. Stinson
Lieutenant, United States Navy
B.S., U.S. Naval Academy, 2009

Submitted in partial fulfillment of the
requirements for the degree of

MASTER OF SCIENCE IN APPLIED PHYSICS

from the

NAVAL POSTGRADUATE SCHOOL
December 2015

Approved by: Dr. Gamani Karunasiri
Thesis Advisor

Dr. Fabio Alves
Co-Advisor

Dr. Kevin Smith
Chair, Department of Physics
Graduate School of Engineering and Applied Sciences

THIS PAGE INTENTIONALLY LEFT BLANK

ABSTRACT

The aim of this work is to develop a metamaterial absorber that can be incorporated into a terahertz (THz) imaging system with a 4.7 THz quantum cascade laser (QCL) illumination source. Finite element (FE) simulations were utilized to design metamaterials, and a Fourier transform infrared spectrometer (FTIR) was employed to characterize the absorption spectrum of each metamaterial configuration. Process parameters for future work with the microfabrication devices have been established for the Naval Postgraduate School clean room. Analysis of experimental data provided insight in determining the refractive index of the metamaterial dielectric, SiO_x, from 3–8 THz and confirmed the Lorentzian shape for the absorption spectrum as theoretically proposed by another group. Future work will incorporate the metamaterial absorber design of this research into a more efficient, cost effective, bi-material THz sensor that can be employed in a variety of naval applications.

THIS PAGE INTENTIONALLY LEFT BLANK

TABLE OF CONTENTS

LIST OF FIGURES

LIST OF TABLES

THIS PAGE INTENTIONALLY LEFT BLANK

LIST OF ACRONYMS AND ABBREVIATIONS

A	Absorption
Al	Aluminum
Ar	Argon
CMA	Canon Mask Aligner
DFT	Discrete Fourier Transform
FE	Finite Element
FTIR	Fourier Transform Infrared Spectrometer
FWHM	Full Width Half Maximum
PPM	Parts Per Million
R	Reflection
RPM	Revolutions Per Minute
SRL	Sensor Research Laboratory
T	Transmission
THz	Terahertz
UV	Ultra-Violet
W	Watt

THIS PAGE INTENTIONALLY LEFT BLANK

ACKNOWLEDGMENTS

I am grateful to have had the privilege to work with Dr. Gamani Karunasiri and Dr. Fabio Alves on this thesis. Their continual support throughout all phases of this research was nothing short of remarkable. Both offered guidance on a daily basis, providing me with the tools to ultimately design, fabricate, test, and analyze a metamaterial in less than a year's time. Their enthusiasm for their work and projects in the NPS Sensor Research Lab is evident every day, and provided me with great motivation for this project.

Dr. Dragoslav Grbovic provided essential guidance during the metamaterial fabrication phase. There was never a time when he was too busy to listen to my thoughts and concerns for the project. Andreas Jacubke's clean room support was vital to the success of this thesis as well.

I appreciate the support of so many wonderful professors, and I am grateful I had the opportunity to pursue my interests in (and out of) the classroom while in Monterey. I would also like to thank Dr. Richard Harkins for his guidance throughout my time at NPS.

Finally, a great thanks to my wife, Hilary, for being my biggest supporter.

THIS PAGE INTENTIONALLY LEFT BLANK

I.   INTRODUCTION

The Sensor Research Laboratory (SRL) at the Naval Postgraduate School has been investigating the use of metamaterials in terahertz (THz) imaging devices. The THz region, typically designated between 0.1-10 x 10^{12} Hz and shown in Figure 1, is in a region that has been designated as the "Terahertz Gap" [1]. This region provides potential for advanced imagery in the security, medical, and communications spheres, along with many others [2–5].

Figure 1.   Terahertz Radiation within the Electromagnetic Spectrum
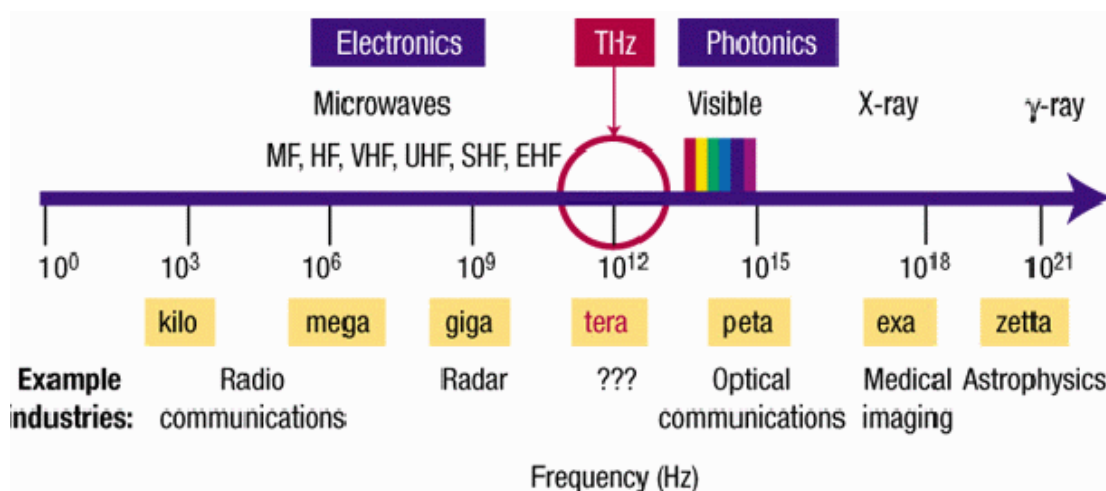
The terahertz region is located between the microwave and infrared regions. Its small wavelength, while still being non-ionizing, makes it ideal for a wide range of imaging and communications applications, along with many others. Source: [6] Coherent InfraRed Center. (n.d.). "Filling the THz Gap," [Online]. Available: http://circe.lbl.gov/ THzGap.html. Accessed Oct. 29, 2015.

THz detectors are desirable since the electromagnetic radiation in this region have the ability to penetrate most non-metallic, non-polar materials, while also having the distinct advantage of being non-ionizing [6]. Due to these distinctive properties, the technology can be utilized for advanced personnel security screening, food inspection, and medical diagnostics, among many other uses [2, 8, 9]. The ability for nondestructive evaluation and inspection is evident over a wide range of materials that exhibit THz spectral characteristics, including human body tissue [3, 10].

The major factors for imaging in the "THz gap" have been low background (thermal) radiation in the THz spectral range and absence of powerful sources and sensitive detectors. The complexity of existing sources and sensors coupled with their high costs has, until recently, prevented widespread use of THz imaging systems. Recent developments in quantum cascade THz lasers and metamaterial-based THz absorbers allow design of compact imaging systems. These metamaterial-based sensor designs, which will be discussed in this thesis, have increased the potential applications in the THz region [8, 10].

Metamaterial absorbers consist of two or more materials arranged in a periodic structure that can absorb THz radiation in a pre-defined spectrum. Metamaterials exhibit different optical properties from their constituent materials, and their ability to be tuned for specific THz frequencies is advantageous for their use in detectors. The mechanism by which metamaterial absorbers behave has been explained using different models, including the resonant circuit model, the plasmonic near-field effect, and Fabry-Perot resonance, etc. [11–14]. Due to the complexity of such structures and their periodic nature, finite element (FE) modeling is the preferable means of designing metamaterials. In order to use metamaterials in sensors, they have to absorb efficiently the incoming radiation on the wavelength of interest. There is a category of planar metamaterials, designated as "perfect absorbers," that can have near 100% absorption within specific frequency ranges. [15]. The metamaterials employed in this work consisted of an aluminum (Al) ground plane, a silicon-rich oxide (SiO_x) dielectric layer, and Al square resonator, all deposited on top of a silicon wafer. An example metamaterial unit cell and periodic array is shown in Figure 2.

Figure 2.   Metamaterial Unit Cell and Periodic Array
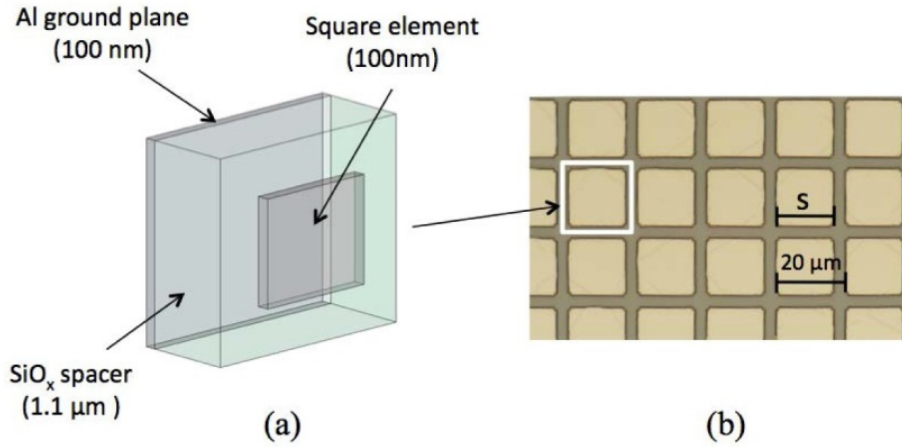
Metamaterial absorber. (a) Basic unit cell with ground plane (Al), dielectric (SiO$_x$) and square element. The square element represents the Al resonator for this research. (b) Array of squares with resonator of size (S) and a pitch of 20μm. Source: [7] Alves et al., "Bi-material terahertz sensors using metamaterial structures." *Opt. Expr.*, vol. 20, no. 11, pp. 13256–13271, May 2013.

The SRL has previously developed bi-material THz devices with integrated metamaterial structures for imaging applications. The absorber portion of the metamaterial device converts incoming electromagnetic radiation to heat, which is then conducted to the bi-material legs of the structure. The legs experience a deformation due to the difference in thermal expansion between the two materials, which is then recorded using an optical readout system [7]. The application of this method across a focal plane array allows for imaging in the THz spectrum.

In order to make the bi-material sensors efficient, absorption has to be optimized; therefore, the objective of this thesis work is to study, design, fabricate, and characterize the planar metamaterial structures previously described. The research is detailed in the following chapters. Chapter II describes the computer simulations and physical assumptions that provided the expected theoretical results for each metamaterial configuration. Chapter III details the metamaterial fabrication process and characterization of the Naval Postgraduate School clean room microfabrication tools. Chapter IV explains the characterization of each metamaterial, and Chapter V provides analysis and discussion of the main results.

THIS PAGE INTENTIONALLY LEFT BLANK

II.   MODELING AND SIMULATION

A.   BACKGROUND

FE modeling and simulations were conducted throughout this research using COMSOL Multiphysics software. The goal was to obtain geometric and physical configurations to maximize absorption of metamaterial for an incoming THz electromagnetic wave. The higher absorption a metamaterial exhibits, the better suited it is for future applicability in THz sensors. In order to study performance of the metamaterial, two different wafers were fabricated with similar configurations. One design consisted of resonators with a constant square size (12 µm) and a varying pitch, ranging from 14 -53 µm. The other consisted of a constant pitch (21 µm) with varying square sizes, ranging from 9–18 µm. Each of their ground planes and dielectric layers were the same. In this document, the varying pitch wafer is designated C-11-31, while the varying square size is designated C-11-34. An overhead representation of wafer C-11-34 can be seen in Figure 3.

Figure 3.   Overhead View of a Wafer Produced with the Varying Square Size Mask
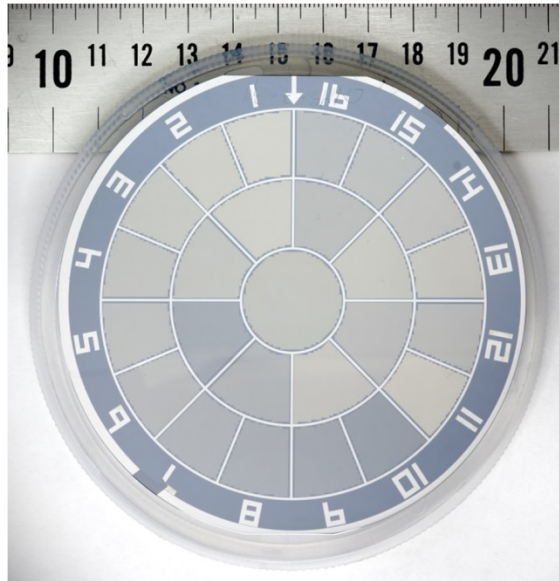
The outer sections for regions 1–10 contained the varying square sizes, ranging from 18–9 µm, all with a constant pitch of 21 µm. Source: [16] B. Kearney et al., "Al/SiO$_x$/Al single and multiband metamaterial absorbers for terahertz sensor applications," *Opt. Eng.*, vol. 52, no. 1, pp. 013801-8–013801-2, 2013.

The FE simulations provided a numerical model for each metamaterial shown in Figure 3 to be compared with corresponding experimental data. The basic unit cell geometry for each simulation is shown in Figure 4. The simulation process consisted of several phases, which included establishing the unit cell geometry, inputting the applicable physical boundary conditions, and evaluating the inputs over a range of specified frequencies. These processes are discussed in detail in the following section.

Figure 4.   Example of the Basic Unit Cell Geometry for COMSOL Simulation
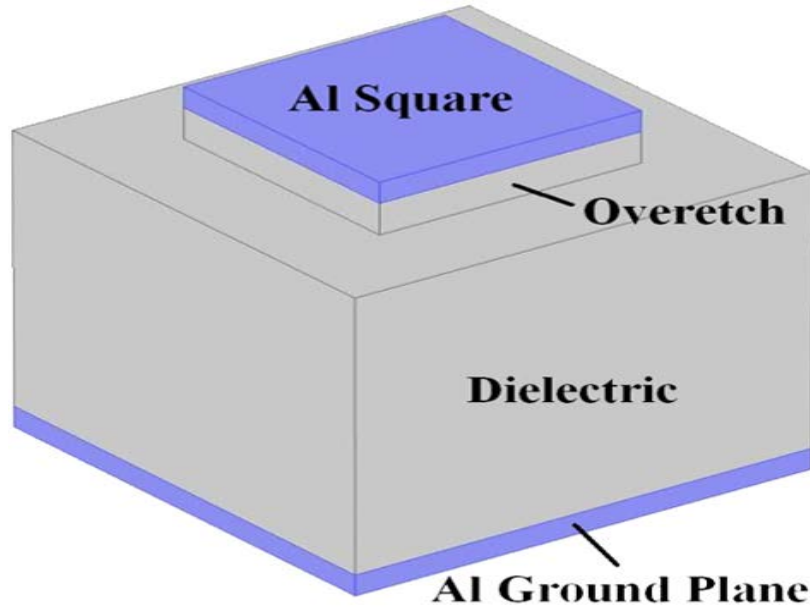
Basic representation of the unit cell geometry for COMSOL simulations. Note that this image does not show the regions of air above and below the cell that are included in the model. Source: [7] Alves et al., "Bi-material terahertz sensors using metamaterial structures." *Opt. Expr.*, vol. 20, no. 11, pp. 13256–13271, May 2013.

B.   UNIT CELL GEOMETRY

The geometry consisted of the Al ground plane, SiO_x dielectric and over etch, and Al square resonator. The over etch was necessary in order to take into account process variations. The surrounding medium (air) for the incoming wave was included as well. The SiO_x dielectric thickness (1.1 µm) was a critical geometric input variable to maximize absorption characteristics and was established from past research in the NPS

SRL [16-18]. Since one desired application for these unit cells is their integration into future designs of thermal sensors in the form of focal plane arrays, it is important to maintain the dielectric thickness as thin as possible to minimize the thermal capacitance. The thermal capacitance is proportional to an objects volume; thus, a thinner dielectric has a smaller volume, which leads to a desirable design parameter in maximizing the sensor's speed of operation [16]. An over-etch layer, which is a result of fabrication limitations, found to have an average thickness of 100 nm. The periodic nature of the planar metamaterial described here allows for simulation and parameter extraction using the repeated unit cell, minimizing simulation run time. Both SiO_x and Al regions in a single unit cell are shown regions (a) and (b) of Figure 5. The geometric regions shown above and below the unit cell are layers of air.

Figure 5.   Unit Cell Layers of SiO_x and Al
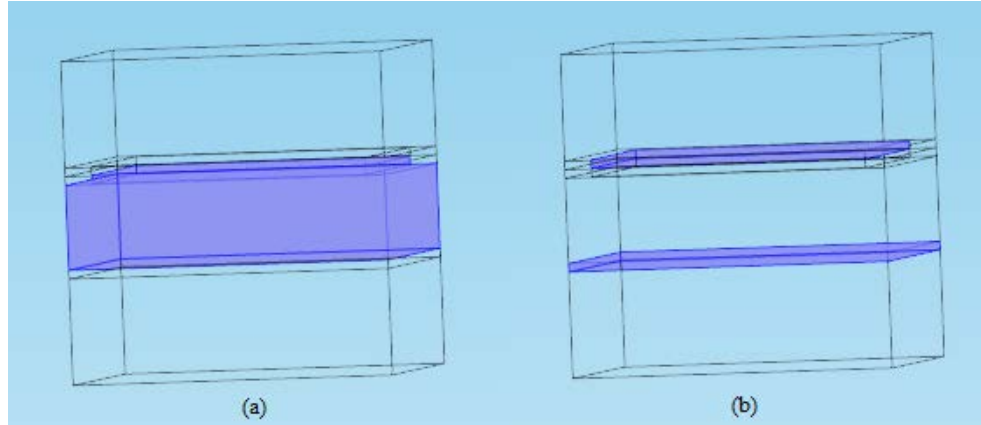
The left cell (a) shows the SiO_x regions, with the dielectric (1.1 µm thick) and over etch (100 nm thick) portions highlighted. The image on the right (b) highlights the Al ground plane and resonator regions (both 100 nm thick). The top and bottom region is air in (a) and (b).

C.   UNIT CELL PHYSICS

1.   Electromagnetic Wave Equation

As discussed previously, the unit cell and surrounding medium consisted of Al, SiO_x, and air. Each material was assigned to its appropriate electromagnetic properties for COMSOL to solve the wave equation for the fields on each mesh node. For a medium

with no charges or initial currents, and where conductivity is not negligible, the EM wave equation is given by

$$\nabla \times \mu_r^{-1}(\nabla \times \overline{E}) - k_0^2\left(\varepsilon_r - \frac{j\sigma}{w\varepsilon_0}\right)\overline{E} = 0 \tag{1}$$

where σ is conductivity, ε_r is permittivity and μ_r is relative permeability [17].

For SiO_x and air, conductivity is negligible and the loss is accounted by the imaginary part of ε_r, therefore COMSOL solves the equation

$$\nabla \times (\nabla \times \overline{E}) - k_0^2 \varepsilon_r \overline{E} = 0 \tag{2}$$

This condition can be set in the model, which reduces the computational efforts needed to perform the calculations. As can be seen by comparing Equation (1) to Equation (2), relative permeability can be set to one for SiO_x. The complex refraction index is given by the following equation

$$\varepsilon_r = (n - ik)^2 \tag{3}$$

where n is the real portion and k is the complex portion. For simulations conducted during this research, n was initially set to 1.9, while k was set to 0.02 [19-20]. The resonant nature of the metamaterial absorption allowed the fitting of the experimental results with FE simulations in order to obtain the refined values of n for SiO_x in the THz range of study.

2. Boundary Conditions

Since the metamaterials for this research are periodic structures, periodic boundary conditions can be used to simulate a unit cell. A further simplification can be done since the metamaterial structures will be used for imaging and sensing and the incident field is near normal [17]. The normal incidence of the incoming wave allows the use of a perfect electrical conductor boundary for the faces perpendicular to the electric field and perfect magnetic conductor for the faces perpendicular to the magnetic field [17]. A schematic diagram of the simulated unit cell is shown in Figure 6.

Figure 6.   Representation of a COMSOL Simulation with Initial Boundary
Conditions
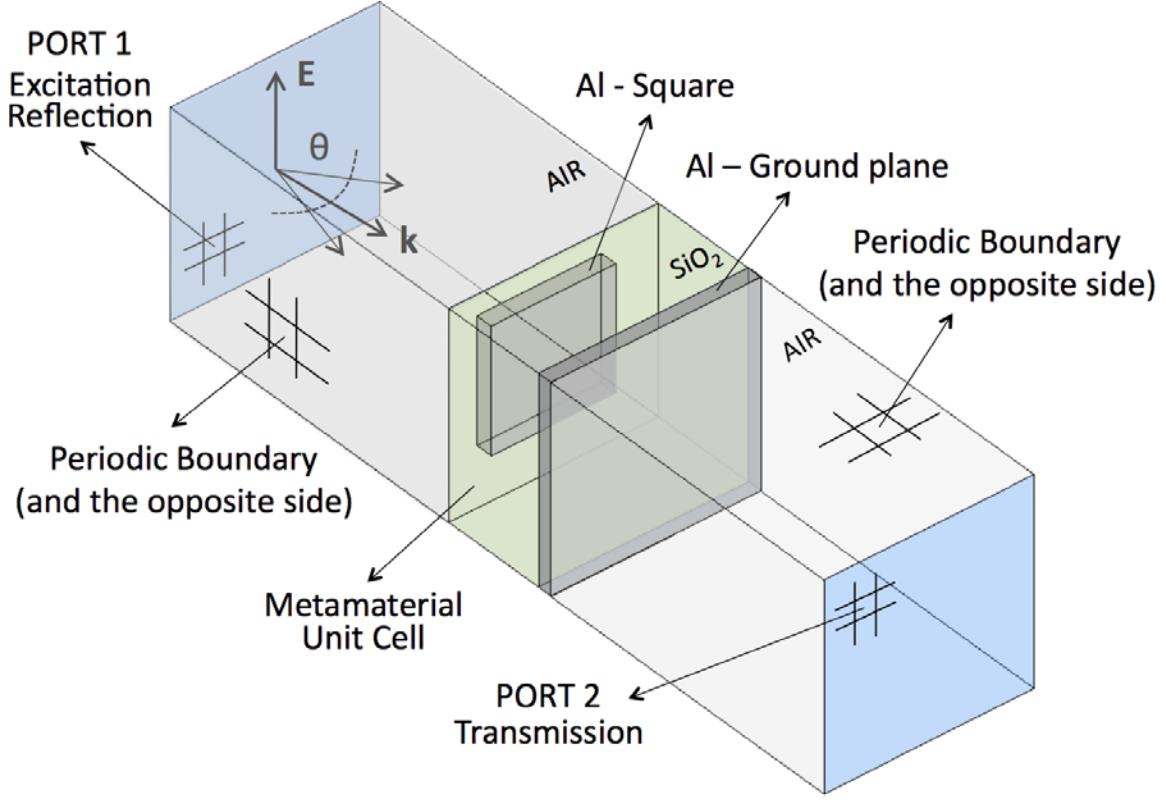
The PEC and PMC are shown by the periodic boundaries and their opposite sides. The incoming wave is incident to Port 1. Notice that there is no transmission through Port 2, due to the thickness of the Al ground plane. Source: [7] F. Alves et al., "Bi-material terahertz sensors using metamaterial structures." *Opt. Expr.*, vol. 20, no. 11, pp. 13256–13271, May 2013.

3.   Input Power

An input power of 1 Watt (W) for the incoming wave was specified for Port 1, depicted by the red incident arrow in Figure 7. Using 1 W for the input power allows the computation of the normalized absorption by calculating the dissipated power on the metamaterial cell [17]. A convenient way to compute absorption is by calculating the amount of reflected power back into the Port 1. Since there is no transmission, absorption is given by

$$A = 1 - abs(S11)^2 \tag{4}$$

where $abs(S11)^2$ represents the reflected power on Port 1 in Figure 6 [7].

9

Particular attention was paid to the meshing at boundaries between different metamaterial layers to ensure the critical boundary interactions were modeled appropriately. After constructing the mesh of each layer horizontally, the sweep function was utilized to create matching in vertical direction within each geometrical configuration. An example of an entire unit cell meshed can be seen in Figure 8.

Figure 8.   Schematic of Unit Cell Meshing
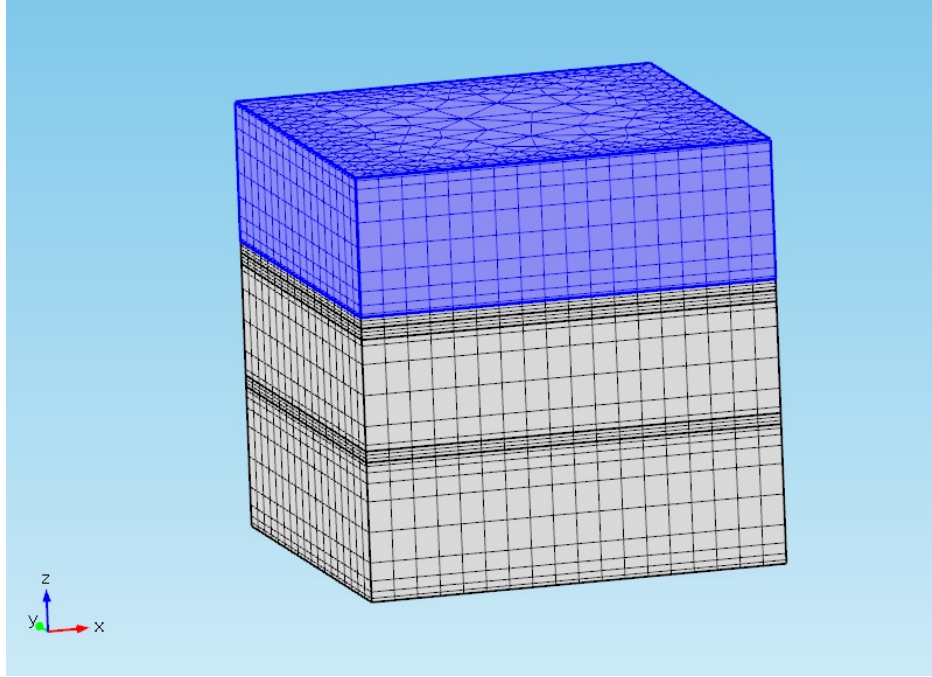
Note that the element intervals at material boundaries are much more detailed than all other elements. This ensures that the COMSOL model accurately outputs the interactions at the critical material interfaces.

D.   EVALUATION

Each simulation was run over a range of THz frequencies that focused around the expected resonance of the particular unit cell. The frequency increment and mesh sizes were the two dominating factors in determining the length of a simulation. For this research, simulation times ranged from 7 minutes to 17 hours. The longer simulations generally employed the parametric sweep function, which varied either resonator size or

Figure 7.   Schematic of Reflection and Transmission
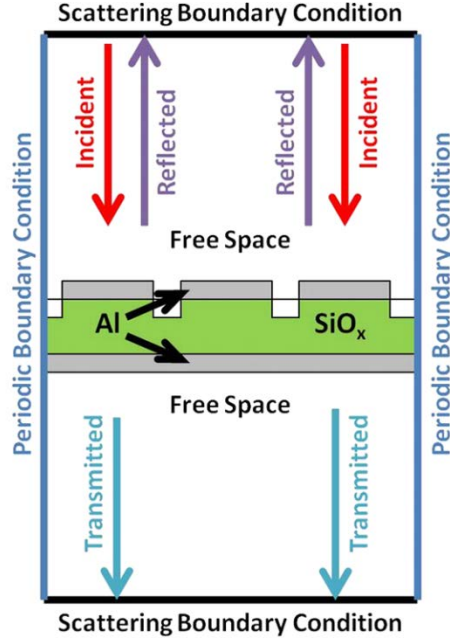
Simple schematic of periodic boundary conditions and scattering boundary conditions. Of note, the thick Al ground plane prevents any transmission. Source: [16] B. Kearney et al., "Al/SiO$_x$/Al single and multiband metamaterial absorbers for terahertz sensor applications," *Opt. Eng.*, vol. 52, no. 1, pp. 013801-8–013801-2, 2013.

4.   Meshing

Meshing generates a set of geometrical nodes for each geometrical region of the unit cell. As a general rule of thumb, the minimum mesh should be no larger than $\lambda/5$ [21]. To be conservative, the largest THz resonant frequency of concern was assumed to be 9 THz, which has a wavelength equal to approximately 30 µm (λ = c/f, where c is the speed of light). Using the meshing constraints, the mesh size should not exceed 6 µm; during all FE simulations, the mesh size was kept below 5 µm. Also of importance, the skin depth for 9 THz was calculated to be 53 nm using the equation

$$\delta_s = \sqrt{\frac{\rho}{\pi f \mu_r}} \qquad (5)$$

where δ_s is skin depth, ρ is resistivity, f is frequency, μ_r is relative permeability [22]. In general, meshing should also have a bare minimum of two elements per skin depth [23].

pitch size, in order to expedite multiple test runs under one simulation. Integrated resistive losses were then utilized to determine the absorption within each metamaterial unit cell.

III. METAMATERIAL FABRICATION

A. FABRICATION BACKGROUND

The clean room at Naval Postgraduate School was utilized to complete the fabrication of the wafer with varying square sizes; it is denoted by C-11-34 in this thesis. Figure 3 in Section II, Part A presents an overhead view of the configuration of this wafer. A clean room, in general, is a room that maintains the atmosphere with a specified particulate concentration through a very fine filtration system and stringent cleanliness controls. A positive pressure is also maintained to minimize the introduction of particulates. The clean room has two sections, one with a particulate concentration of 1,000 parts per million (PPM) and the other 10,000 PPM.

The wafer had the Al/SiO$_x$/Al layers deposited at the facilities of Oak Ridge National Laboratory. Each Al layer was 100 nm thick, and the SiO$_x$ layer was 1.1 µm thick. Multiple test runs were completed prior to the final fabrication of wafer C-11-34. These test runs were necessary to tune the required processing steps and produce a sample that complies with the design specifications.

B. FABRICATION PROCESSES

The process steps include photolithography, development, etching, and removal of photoresist. Each is detailed in the following text.

1. Preparation for Lithography

The wafer is first placed in the Brewer Science CEE 200X Spin Coater, which can be seen in Figure 9. After verifying the proper recipe is loaded in the spin coater, the wafer is centered. MCC 80/20 Primer was then pipetted on the wafer surface and spun for 45 seconds at 3,000 revolutions per minute (RPM) to ensure an even distribution of the primer. A positive photoresist, SPR 955-CM-0.9, was then pipetted onto the wafer and span for another 45 seconds at 3,000 RPM to ensure a uniform coating of 0.9 µm is achieved. The wafer was then placed onto a hot plate set to 90 ºC for 90 seconds, after which it was placed on a metal plate to cool down. The hot plate and metal heat

conducting plate are shown in Figure 10. All of these processes remained constant for each test run and the fabrication of C-11-34.

Figure 9.   Brewer Science CEE 200X Spin Coater

The spin coater distributed the MCC 80/20 Primer and the SPR 955-CM-0.9 Photoresist along the wafer during the pre-lithography phase of fabrication.

Figure 10.   Hot Plate and Heat Conducting Plate Used for the Pre-Exposure Bake
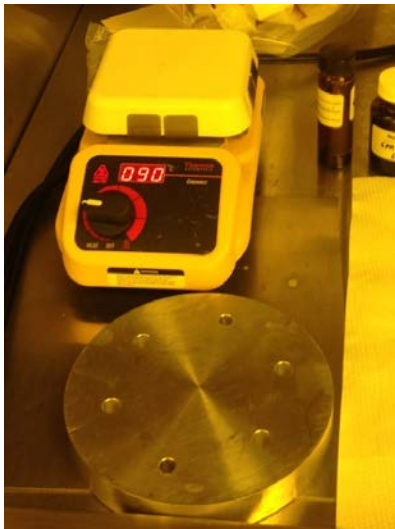
The hot plate was used during the pre-exposure and post exposure bakes. The metal plate (located below the hot plate) let the wafer cool to room temperature immediately after the bakes.

2. Lithography and Post-Exposure bake

The PLA-501 S Canon Mask Aligner (CMA) is utilized to align the wafer with the desired mask and expose the unmasked areas to the ultra-violet (UV) light The CMA can be seen in Figure 11. Exposure time is determined by the light integra setting, located on the CMA main panel. The light integra settings tested prior to final fabrication ranged from 120 to 100. The setting of 120 was approximately 10 seconds of UV exposure, while the setting of 100 was approximately 8 seconds. Since SPR 955-CM-0.9 is a positive photoresist, the UV light weakens the portions of the photoresist not covered by the mask. This leads to the mask pattern being the same pattern as that of the wafer upon the completion of the fabrication process.

The other variables adjusted with the CMA were print gap and align gap, which are located on the horizontal display panel of Figure 11. Align gap determines the initial alignment parameters while print gap, measured in μm, adjusts the distance of the mask from the wafer directly before exposure initiates. Having the mask further away from the wafer can increase the diffraction effects causing unresolvable features. Figures in the Appendix, Part B show examples of test runs with the results using a larger print gap. Placing the mask too close must also be avoided because it can lead to small deposits of photoresist on the mask if the photoresist is not spread evenly following the spin cycle. For this reason, the print gap was never less than 5 μm, which was the setting for the final fabrication.

The wafer was then transferred onto the hot plate for the post-exposure bake. For this bake, the hot plate was set to 120 ℃ for 90 seconds. Initially, only light integra settings were adjusted between test runs. The results from initial test runs led to the print gap being adjusted to 10 μm. The tables in the Appendix, Part A detail the adjustments made between all test runs, while Table 4 shows the final parameters for the fabrication of C-11-34.

Figure 11.   PLA-501 S Canon Mask Aligner

The CMA was used to expose each wafer with UV light during the photolithography process.

3.   Development

The development solution was Microposit MF-CD-26 Developer (CD-26), an alkaline corrosive utilized to remove the exposed photoresist from the wafers. CD-26 was placed in a plastic container with sufficient capacity to place the wafer within it. Development time is the amount of time the wafer stays in CD-26 solution after the post-exposure bake. During the development process, portions of the SPR 955-CM-0.9 that were not exposed to UV light dissolve off the wafer and into the solution. Over-development can dissolve portions of the photoresist that were exposed to UV light, leading to the features having smaller than desired dimensions. To produce the desired dimensions, it is important to pull the wafer out of the CD-26 solution as soon as all the exposed photoresist is off the wafer. Several test runs were conducted and optical microscopy was used to analyze resultant resonator dimensions and features. In the actual fabrication of C-11-34, a development time shorter than the test runs was used, as shown in Table 4.

4. Etching

Wafer C-11-34 underwent Argon (Ar) sputter etching with the Oxford Instruments PlasmaLab System 100, as shown in Figure 12. Sputter etching is the process of removing unprotected material by using an inert gas (Ar). In the case of this research, this process should remove approximately 100 nm/min of Al based on previous work in the NPS clean room. Prior to etching, the thickness of SPR 955-CM-0.9 in various regions of the wafer was measured using an optical microscope coupled with the FILMeasure program. This program specifically utilized the Filmetrics F40 tool to measure the thickness of a film (SPR 955-CM-0.9) on a metal (Al), although it can be set up to measure a variety of film and metal combinations. The initial thickness of photoresist was on average 877 nm, as expected for SPR 955-CM-0.9.

The first sputter etch cycle was one minute in duration, after which Filmetrics F40 was again utilized to measure the SPR-955-CM-0.9 thickness. The KLA D-120 Tencor Profilometer was used to measure the combined thickness of the metal and the film. Similar to the Filmetrics measurements, it measured several different portions of the wafer. The selected areas transitioned from regions with photoresist directly to regions where photoresist had been removed during the development process. A height histogram from the Tencor Profilometer is shown in Figure 13.

Figure 12.   Oxford Instruments PlasmaLab System 100 Used for Sputter
Etching Wafer C-11-34
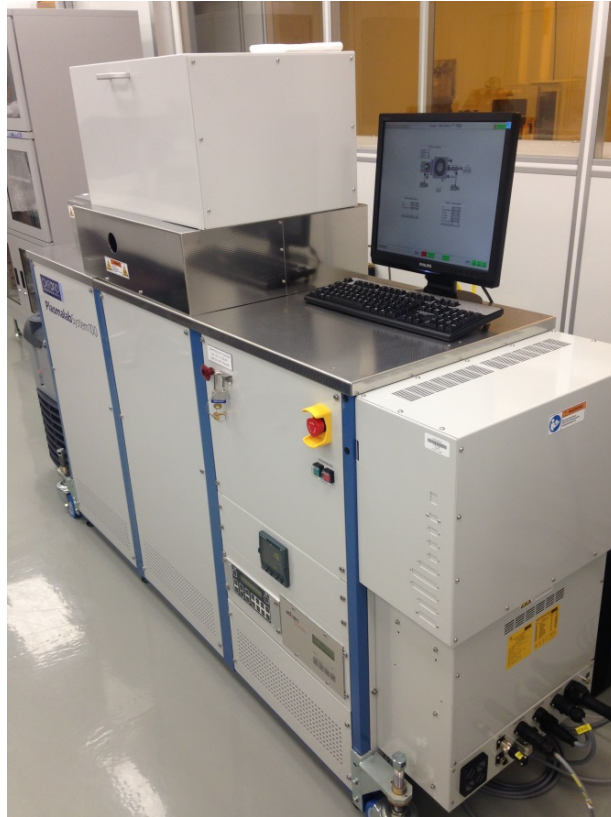
Used for the Ar Sputter Etching of Wafer C-11-34. Two etches, both one minute in
duration, were required to remove the requisite amount of aluminum to fabricate the
desired metamaterial. Fabrication limitations led to the over etch being approximately
100 nm.

Figure 13.   Height histogram from the KLA D-120 Tencor Profilometer of C-11-34 prior to final Sputter Etch
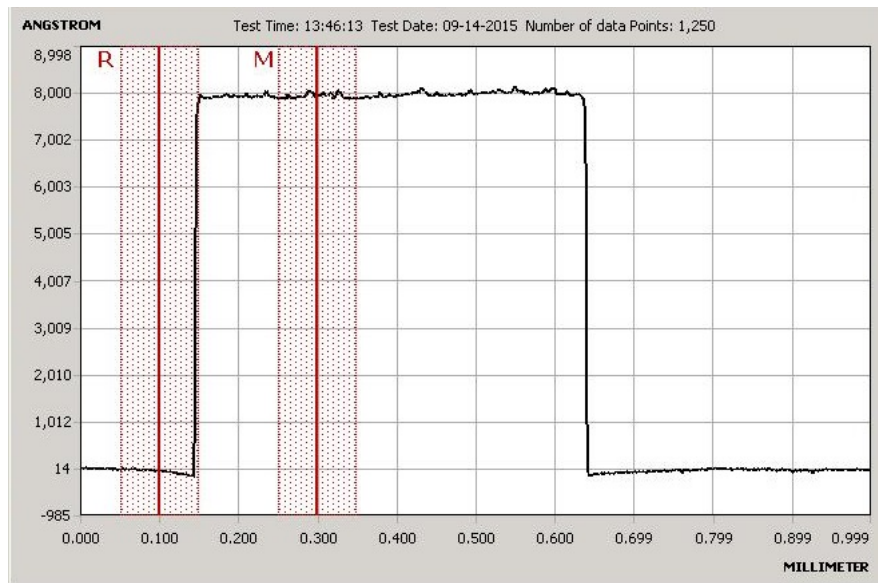
The difference in height between the peak region and baseline region provides the total thickness of aluminum and photoresist over a specified region. Combining this data with the FILMeasure program provides the Al thickness removal for each sputter etch cycle.

The difference between the measured thicknesses from the Tencor Profilometer (Al + SPR 955-CM-0.9) and FILMeasure program (SPR 955-CM-0.9) provides the thickness of aluminum removed during each sputter etch cycle.

Two sputter etch cycles were required for the fabrication of wafer C-11-34. Table 1 contains the Al and SPR 955-CM-0.9 thicknesses before and after the first etch, while Table 2 contains the thicknesses after the second etch. Region I was near the edge of the wafer and Region II was near the center of the wafer. These regions were selected for final analysis as they were measured consistently between each process cycle. An average Ar sputter etch rate can be utilized for future NPS clean room work for both photoresist and aluminum from these tables.

19

Table 1.   Etching Results for First Cycle (60 s) of Ar Sputter Etching Wafer
C-11-34

Region	SPR 955 Thickness (nm) before 1st etch	SPR 955 Thickness (B) (nm) after 1st etch	Δ SPR 955 thickness (nm) after 1st Etch	SPR 955 + Al thickness (A) (nm) after 1st etch	Amount of Al etched (A-B) (nm) after 1st etch
I	813	720	97	759	39
II	941	828	113	875	47
Average	877	774	105	817	43

The SPR 955-CM-0.9 thickness (B) was determined using the Filmetrics program, while the combined thickness of SPR 955-CM-0.9 and Al (A) was determined with the Tencor Profilometer. Taking the difference between A and B yielded the amount of Al etched during each sputter etch cycle.

With the deposition thickness of the top aluminum layer being 100 nm, it was unavoidable to not slightly over etch into the SiO_x, as depicted visually in Section II, Part A., Figure 4. A slight over etch ensures that the area surrounding the resonator is air; otherwise the final fabricated metamaterial would not have the intended absorptive properties. This effect also contributes to the metamaterial's configuration, specifically the size of Al resonator, having a slight difference with the mask resonator sizes, detailed in Table 4.

Table 2.   Etching Results for Second Cycle (60 s) of Ar Sputter Etching
Wafer C-11-34

Region	SPR 955 Thickness (nm) before 2nd etch	SPR 955 Thickness (B) (nm) after 2nd etch	Δ SPR 955 thickness (nm) after 2nd etch	SPR 955 + Al thickness (A) (nm) after 2nd etch	Amount of Al etched A-B (C) (nm) after 2nd etch
I	720	619	101	761	142
II	828	720	108	884	164
Average	774	669.5	104.5	822.5	153

The SPR 955-CM-0.9 thickness (B) was determined using the Filmetrics program, while the combined thickness of SPR 955-CM-0.9 and Al (A) was determined with the Tencor Profilometer. Taking the difference between A and B yielded the amount of Al etched during each sputter etch cycle.

5. Removal of Photoresist

The last process step prior to FTIR testing was the removal of the remaining photoresist with the Trion Sirius T_2 Reactive Ion Etcher, shown in Figure 14. The recipe, called the "Clean" recipe for this research, was set with an RF power of 150 W, a pressure of 250 millitorr and O_2 flow set at 50 standard cubic centimeters per minute. Using this recipe in the etcher for 60 seconds reduced the SPR-955-CM-0.9 thickness on average 516 nm. To complete the process, the wafer was placed back in the Sirius T_2 for thirty seconds to remove the remaining photoresist. The complete results for SPR 955-CM-0.9 removal rates in the Sirius T_2 are shown in Table 3.

Table 3.   SPR 955-CM-0.9 Removal Rate

Region	SPR 955 thickness Prior to Ion Etch (nm)	SPR 955 thickness After 60 (s) Ion Etch (nm)	Δ SPR 955 thickness (nm)
I	619	181	438
II	720	126	594
Average	669.5	153.5	516

The Trion Sirius T_2 Reactive Ion Etcher completed the removal of The SPR 955-CM-0.9 after the sputter etch process.

21

Figure 14.   Trion Sirius T$_2$ Reactive Ion Etcher

The "Clean" Recipe was used during the final process step in the removal of SPR 955-CM-0.9 photoresist. Conditions were as follows: RF power of 150 W, pressure of 250 millitorr and O$_2$ flow of 50 standard cubic centimeters per minute.

C.   POST-FABRICATION ANALYSIS

Using an optical microscope coupled with the Olympus DPController program, resonator square sizes were determined for each test run and for the fabrication of wafer C-11-34. The DPController program captures images from the optical microscope with a magnification up to 1000X, and allows for the observation of the general characteristics of each fabricated wafer. The values obtained from the final fabrication can be compared to the mask size in Table 4. The actual measured resonator sizes using the DPController program from all the trial runs are shown in the Appendix, Part A. Part B of the Appendix contains all images of the test run resonators taken with the DPController program. Figure 15 provides an image of metamaterial with 17 μm squares during the first test run. It can be seen that the square size is larger than expected (17.5 μm), squares are interconnected, and evidence of light diffraction around the mask (the greenish-blue regions around the dark squares). Figure 16 shows an improvement from Figure 15 but the diffraction is much more evident, with the

exposure time established through the light integra setting. After several test runs, the fabrication of wafer C-11-34 produced much more consistent square sizes throughout the tested regions (with no evidence of diffraction or waviness seen during test runs), as shown in Figure 17.

Figure 15.   Pre-Fabrication Test Run #1, Wafer C-11-34, 17 µm Square
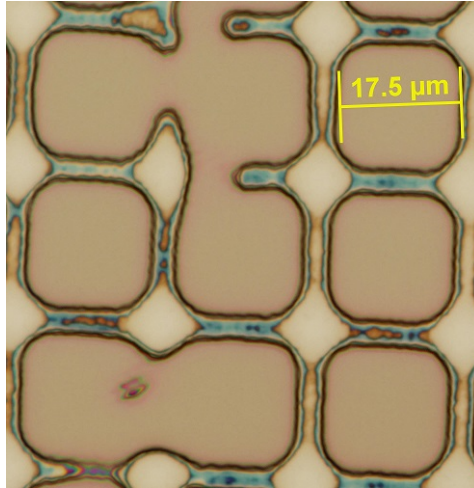
Notice that several resonators are interconnected due to an exposure time that was too short. The light blue color surrounding the resonators is caused by light diffraction from too large a print gap.

Figure 16.   Pre-Fabrication Test Run #2, Wafer C-11-34, 17 µm Square
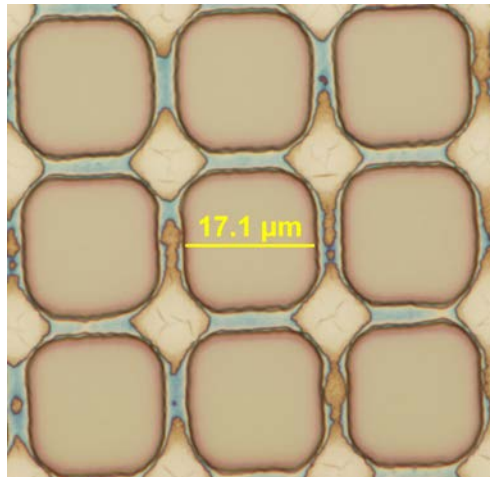
With a slightly longer exposure time, Test Run #2 did not have any connected resonators, but the large print gap created a significant diffraction pattern around the resonator.

Figure 17.   Fabrication of C-11-34, 18 um Square
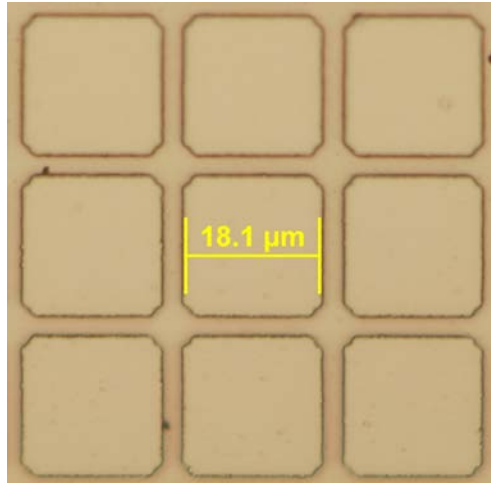
Note the well-defined resonator features for Wafer C-11-34, as compared to the test runs.
The dimension of the resonator, 18.1 µm, is very close to the measured mask square size
of 18.0 µm.

Table 4.   Final Parameters Used for Fabrication of Wafer C-11-34

Mask Unit Cell Size (µm)	Actual Unit Cell Size	Light Integra Setting	Print Gap (µm)	Align Gap (µm)	Development Time (s)
18	18.1	120	5	40	20
17	17.1	120	5	40	20
16	16.1	120	5	40	20
15	15.1	120	5	40	20
14	14.1	120	5	40	20
13	13.1	120	5	40	20
12	12.1	120	5	40	20
11	11.1	120	5	40	20
10	10.1	120	5	40	20
9	9.2	120	5	40	20

Note that the development time in CD-26 was reduced to 20 seconds from previous runs
to minimize over-etching.

IV. EXPERIMENTAL DATA COLLECTION

A. FTIR FUNDAMENTALS

The following section will discuss the physical makeup of the Fourier Transform Infrared Spectrometer (FTIR) and the accessories used during this research. It will also explain the basics of the FTIR's operation.

1. Background

An FTIR was used to measure the reflectivity of the fabricated metamaterial wafers. The FTIR employed was a Thermo-Nicolet Nexus 870 with a deuterated triglycine sulfate pyroelectric detector with a polyethylene window fitted with a Pike MappIR accessory. The MappIR accessory allows for transmission (T) and reflection (R) to be measured along the THz frequencies of interest for this research (1.5-18 THz), allowing absorption (A) to be calculated by

$$A = 100 - R - T \tag{6}$$

2. FTIR Operation

The FTIR is made up a Michelson interferometer with an arm containing a moving mirror. This mirror creates periodic oscillations in amplitude, whose frequency is dependent on the mirror's velocity and the radiation's wavelength. This movement allows the FTIR to obtain simultaneous frequencies by using a discrete Fourier transform (DFT) [17]. The moving mirror also leads to a phase difference between the two wavelength dependent light paths, from which the FTIR outputs the variation of intensity *(I)* as path distance (Δy) changes [17–18]. The relationship between intensity and path distance is given by the equation (where σ is the wave number)

$$I(\Delta y) = \int_0^\infty I(\Delta y, \sigma) d\sigma = \int_0^\infty (E_o^2(\sigma)/2) \, d\sigma + \int_0^\infty (E_o^2(\sigma)/2) \cos(2\pi\sigma\Delta y) \, d\sigma \tag{7}$$

The FTIR is able to output specific transmission data for given frequencies by taking the Fourier transform of the second term, known as the interferogram, in Equation (7) [18]. Since the phase difference between the two light paths is wave dependent, the FTIR can obtain discrete transmission data employing a broadband IR source [18].

A reflection background measurement is taken with a gold mirror before each measurement. Despite the FTIR being purged by dry air, it is important that a new background be taken prior to each measurement collection period in order to remove the inconsistent spectral characteristics of the system [17]. The OMNIC program, discussed in the following section, compares the spectral characteristics of each sample with the background measurement to provide consistent reflection data that can be used to extract THz absorption of metamaterial.

B. FTIR DATA COLLECTION METHOD

The FTIR data collection method consisted of two steps. The first was setting up the complementary programs for the FTIR, OMNIC and AutoPRO. The second was the physical setup of the FTIR and complementary accessories to ensure the designated region of the metamaterial is aligned with the FTIR beam.

1. Complementary Programs: OMNIC and AutoPRO

The two programs that facilitate the measurements from the FTIR are OMNIC and AutoPRO. OMNIC provides the ability to adjust the input parameters, such as the velocity parameter and the spectral range. The velocity parameter determines the speed (cm/s) of the moving arm in the interferometer, while the spectral range, identified by wave numbers from 50 to 600 units, establishes the analyzed frequency spectrum from 1.5 to 18 THz as seen in Figure 18 [18]. AutoPRO controls the movement of the MappIR tray that aligns the desired portion of the test wafer with the aperture of the FTIR. Figure 19 shows the AutoPRO Control Main Menu, which is used to load, unload, and to position the wafer under the FTIR aperture. A compressor must also be running to purge the FTIR with clean, dry air to maximize both the internal optics and the measured signal to noise ratio (SNR) [17].

Figure 18.   OMNIC Setup Parameters Window
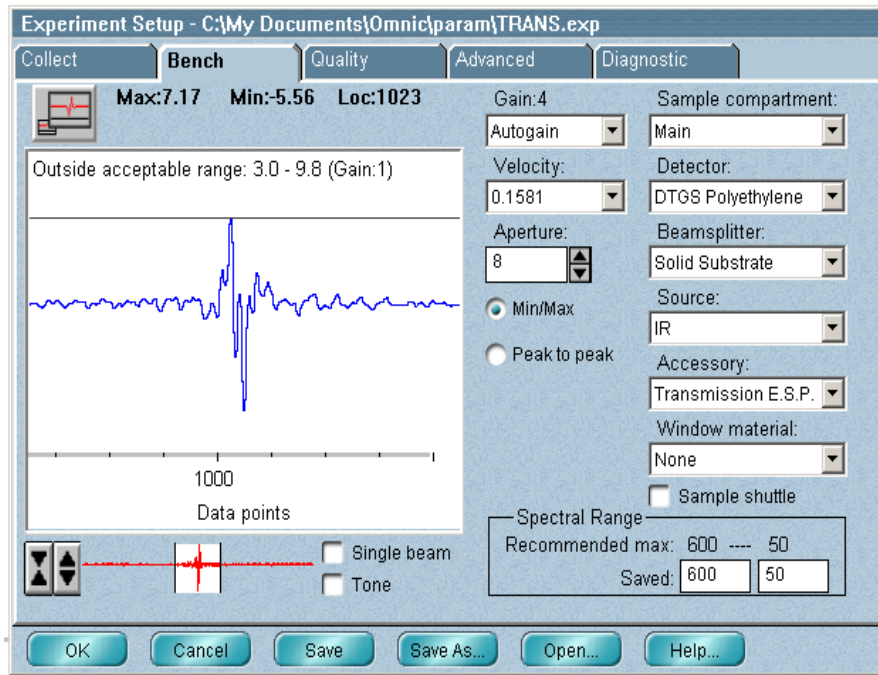
Parameters utilized for FTIR testing of fabricated metamaterials. Of note for the bench parameters, the velocity establishes the speed of the interferometer's moving arm and the spectral range determines the frequency spectrum, which correlates to 1.5-18 THz.

Figure 19.   AutoPRO Control Window
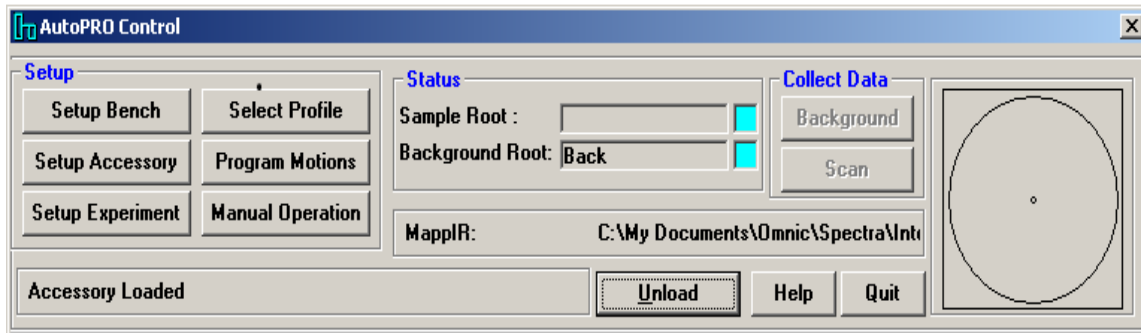
The control window allows the user to load, unload, and accurately align the desired portion of the metamaterial with the FTIR aperture. For this research, the aperture was aligned with the center of wafer, as depicted with the small circular region seen in the far right portion of this figure.

2.   Measurement Procedures

The metamaterial measurement procedures consisted of the setup stage and testing stage. During the setup phase, it was critical that the FTIR was set to the proper

mode, while during the testing phase it was important that the wafer be handled delicately to prevent it from breaking.

a. Setup

The MappIR accessory allows FTIR measurements to be taken in either the reflection or transmission mode, as illustrated in Figure 20. The setup shown in (a) measures the amount of reflected THz energy from the wafer that is placed on the MappIR tray, while the setup in (b) measures the energy transmitted. The metamaterial Al ground plane layer, with a deposited thickness of 100 nm, prevents transmission of all spectral ranges analyzed for this research. Since 1 THz equates to a skin depth of approximately 80 nm for Al, all measurements of metamaterials are collected in the reflection mode [17]. Prior to collecting measurements via reflection mode, though, it is necessary to verify proper operation of the FTIR by placing the MappIR in transmission mode. Verification is done through the Bench setting in the OMNIC program, as seen with the waveform in Figure 18.

Figure 20.　Schematic of FTIR Modes
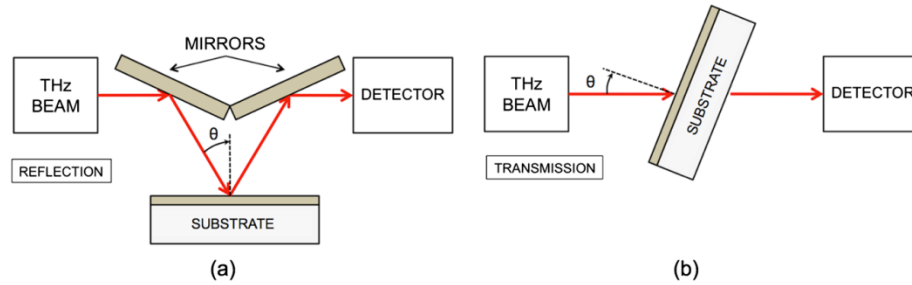
Mode (a) demonstrates the basic operation for metamaterial testing, while mode (b) is used to verify proper operation of the Bench setting in the OMNIC program prior to testing. Source: [18] A.T. Phillips, "Resonant terahertz absorption using metamaterial structures," M.S. thesis, Appl. Phys. Dept., Naval Postgraduate School, Monterey, CA, December 2012.

b. Testing

Once proper operation of the FTIR is verified, a background sample is taken with a gold plated wafer in the reflection mode. Once the background is established in the Collect settings within OMNIC, reflection data can be collected by positioning the wafer

in the MappIR Tray and placing the FTIR in reflection mode. Figure 21 shows the collected background and reflection of several regions of wafer C-11-34. Since we have already proven there is no transmittance through the wafer, Equation 6 can neglect the T and becomes

$$A = 100 - R \tag{8}$$

The reflection data collected by OMNIC can be converted into absorption by using Equation (8).

Figure 21.   OMNIC Data Collection Window
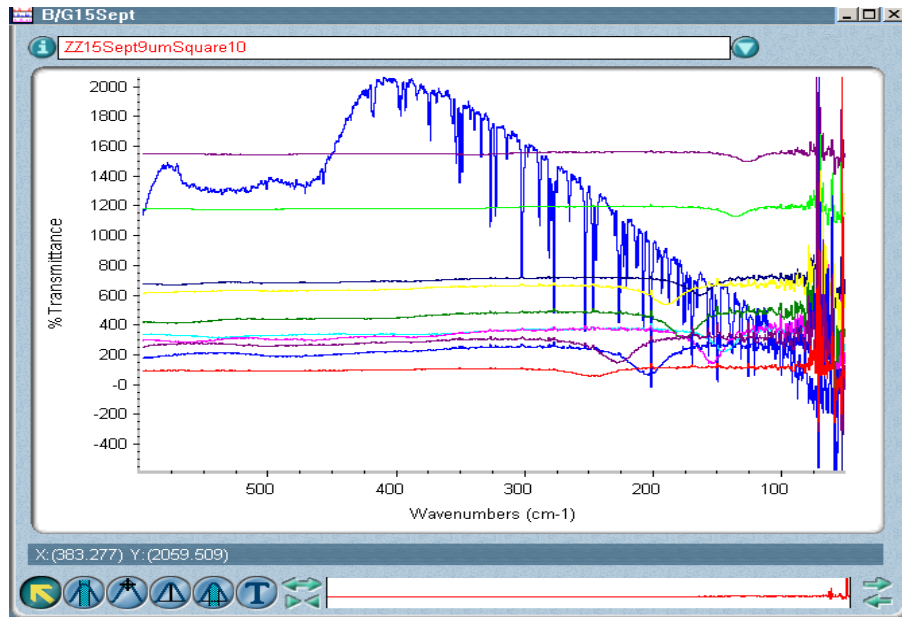
Measurements from regions 1–10 of Wafer C-11-34, depicted by the generally smooth colored lines with singular inverse reflection peaks. Note the background measurement in blue. Although the X-axis is labeled as % transmittance, the FTIR is actually providing a reflection output since the MappIR accessory is set to reflection mode.

THIS PAGE INTENTIONALLY LEFT BLANK

V.   ANALYSIS

A.   CONSTANT PITCH, VARYING SQUARE SIZE METAMATERIAL

The first metamaterial configuration discussed will be the constant pitch (21 µm), with a variable resonator square size, designated in this text as Wafer C-11-34. The resonator square sizes ranged from 18 µm to 9 µm, in increments of 1 µm.

1.   General Observation of C-11-34

The measured absorption as a function of THz frequency for C-11-34 is shown in Figure 22. General observation shows several interesting characteristics for this metamaterial with respect to resonant frequencies and absorption values. Also of note, there are several resonant modes for each metamaterial. The main mode for all configurations under study is located within 3 to 8 THz, with at least one more mode observable for each configuration. While these modes at frequencies greater than 10 THz have lower absorption, their presence can be related to coupling between square elements and other factors that require further study [24]. This research was primarily focused on the main mode for each metamaterial as shown in Figure 23.

Clearly, the resonant frequency increases as the resonator square size decreases. If we assume that the resonant absorption in a metamaterial can be described by a RLC model [11, 18], then resonant frequency (ω_o) can be related to inductance (L) and capacitance (C) by the following equation

$$\omega_o = \frac{1}{\sqrt{LC}} \tag{9}$$

where C is given by the equation

$$C = \varepsilon A / d \tag{10}$$

where A is proportional to the area of the square, ε is the dielectric constant of SiO_x, and d is the thickness of dielectric (SiO_x) layer. From these equations, it is possible to infer

31

that the resonant frequency is inversely proportional to the square size, which agrees well with the measurements as shown in Figure 24. The linear fit in Figure 24 is given by

$$F = .2072 + 65.96(1/s) \qquad (11)$$

where s represents the square size in µm and F is frequency in THz. This relation can be used to estimate square size needed for a desired frequency in the frequency range. Further analysis must be conducted to verify the accuracy of Equation (11) for extrapolating into the infrared and or visible range.

Figure 22.   Absorption vs. Frequency for Constant Pitch, Varying Square Size Metamaterial (C-11-34)
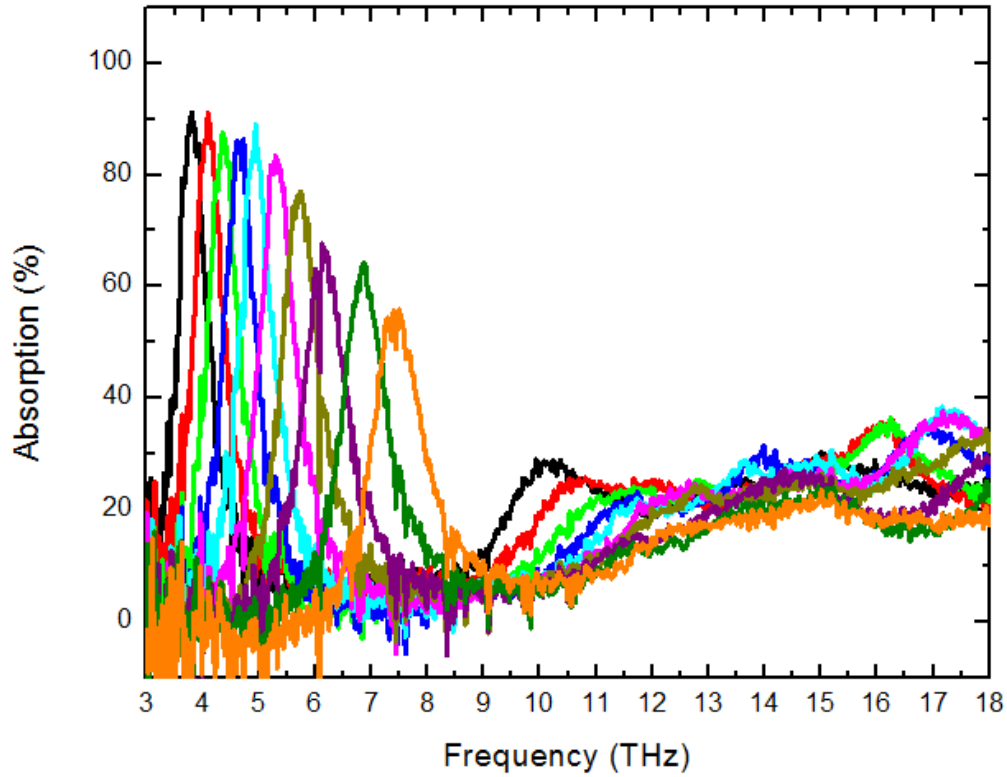
Absorption as a function of THz frequency for Wafer C-11-34, with resonator square size ranging from 18 µm to 9 µm. The pitch (21 µm) was held constant for each region. Each curve represents decrease of square size by 1 µm, starting with the 18 µm resonator (black curve) through the 9 µm resonator (orange curve). As the square size decreases, there is a mostly steady decrease in peak absorption, while peak frequency increases. Although this research is primarily focused on the primary mode between 3–8 THz, note the other modes from 10–18 THz with lower absorption peaks.

Figure 23.   Main Mode Absorption vs. Frequency for Constant Pitch, Varying Square Size Metamaterial (C-11-34)
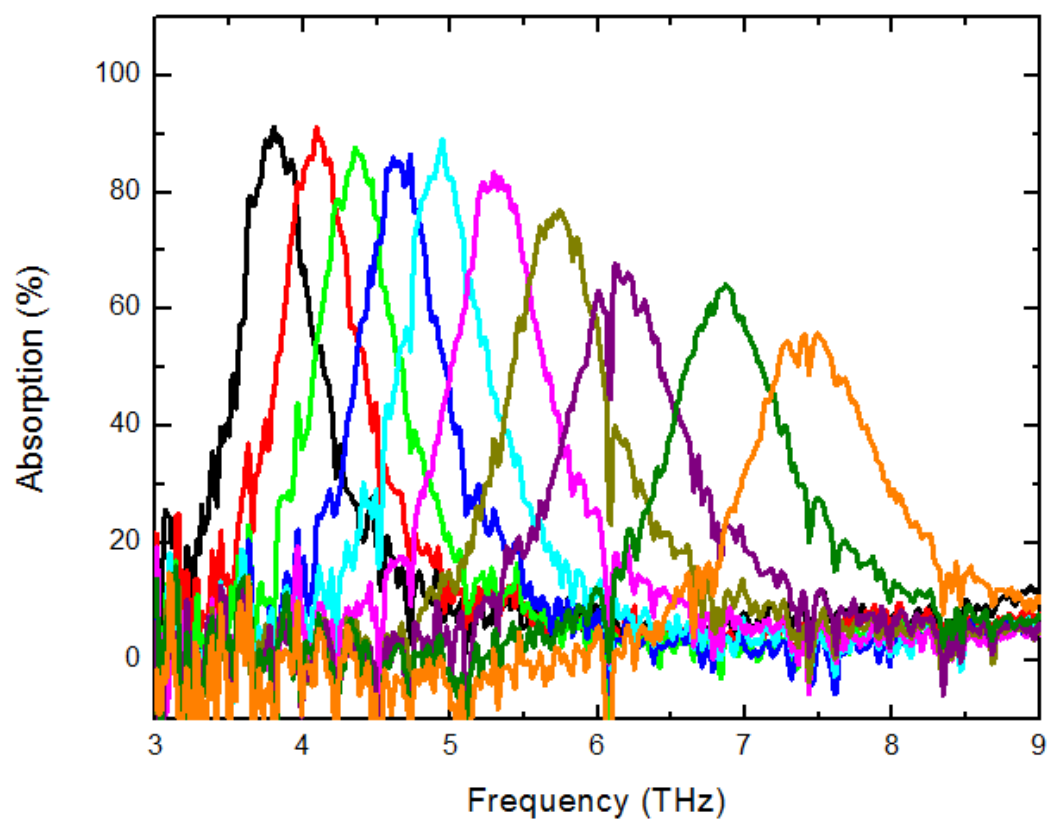
Absorption data for the main mode of C-11-34. Note the shift in peak absorption frequency from the 18 µm square (black curve) to the 9 µm square (orange curve).

Figure 24.   C-11-34 Frequency vs. Inverse Square Size
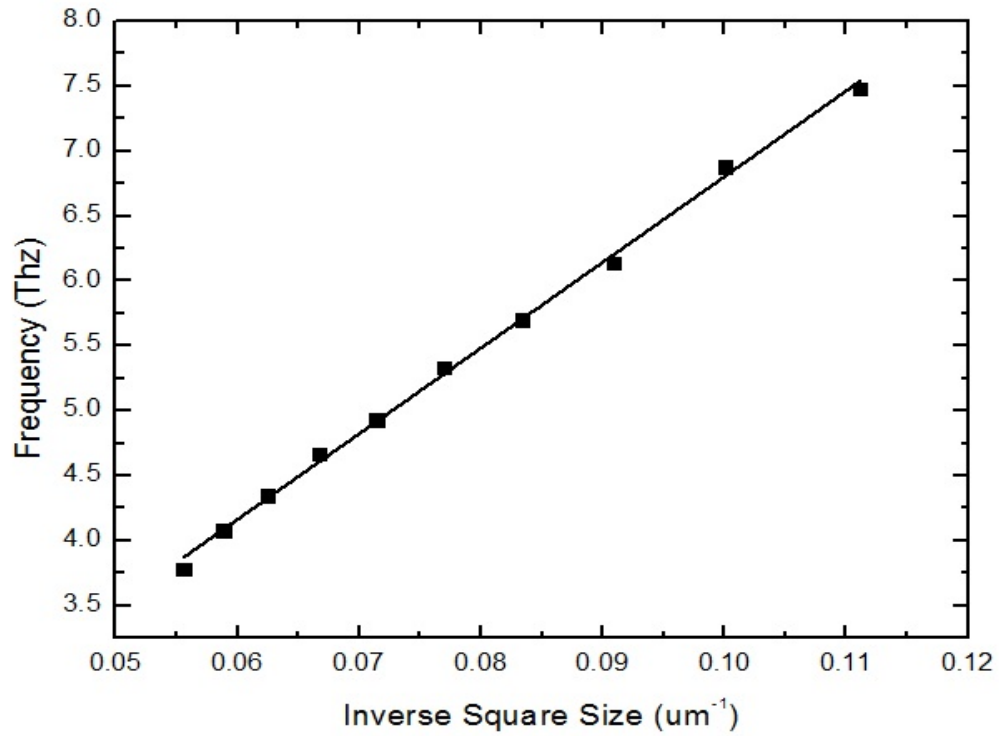
Frequency with respect to the inverse of the resonator square size follows a mostly linear trend. Using a RLC model, an increasing square size increases the overall capacitance through its larger area; therefore, the smaller the resonator, the higher the resonant frequency. The linear fit is given by the following equation: $F = 0.2072 + 65.96(1/s)$, where s is the square size (μm) and F is frequency in THz.

2. Absorption Characteristics of C-11-34

Maximum absorption occurred for the 18 µm resonator. As square size decreased, peak absorption generally decreased. Physically, the 18 µm resonator has the smallest gap between unit cells. It also has the largest fill factor, which is a dimensionless ratio between the area of the Al resonator square and the total unit cell area. It is clear that as fill factor also goes down peak absorption goes down as shown in Figure 25.

Interestingly, though, the total absorption under each curve was relatively constant for all square sizes. Within the first mode for all metamaterials, a slight broadening of each absorption curve is evident as the peak absorption decreases. Despite the reduction of peak absorption as the square size decreases, the broader curves lead to a relatively constant area under each curve, when the integral is taken from across the main mode. Figure 26 shows an integrated absorption of about 70 in units of %.THz for all samples except for the one with a square size of 18 µm.

Figure 25. C-11-34 Peak Absorption vs. Fill Factor and Gap
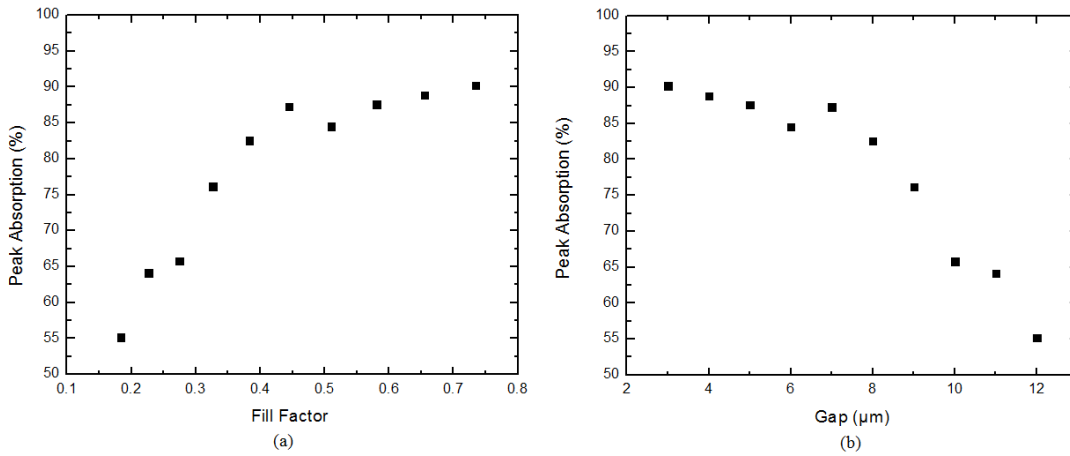
Fill factor (a) is the dimensionless ratio of the area of the resonator vs the area of the unit cell, while gap (b) is the distance between each unit cell. A larger fill factor clearly leads to higher peak absorption. Conversely, a larger gap, and thus a smaller fill factor, leads to a smaller peak absorption.

Figure 26.   C-11-34 Area Under Absorption Curve vs. Fill Factor
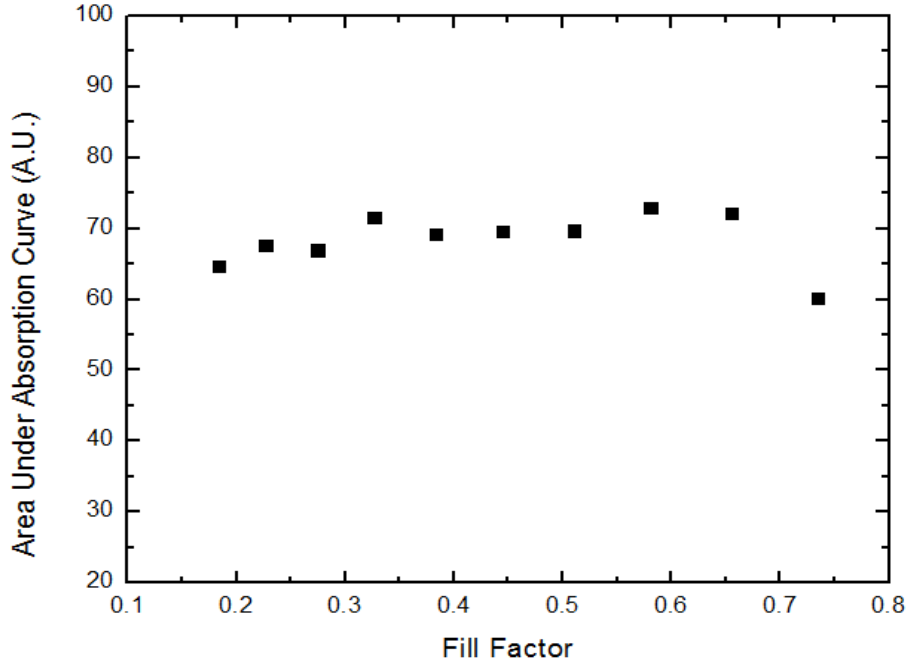
The area under the absorption curve can be seen to be relatively constant for all metamaterials with the resonator square size from 18 μm to 9 μm. This is somewhat evident through inspection of Figure 23; as peak height decreases, the full width half maximum increases.

a.   Refraction Index Dependent on Frequency

The experimental data was compared to the initial COMSOL simulations, showing that simulated and measured peak absorption frequency values were slightly off. Since all geometric parameters in COMSOL were the same as C-11-34, conductivity of Al is high ($>10^7$ S/m) and the SiO_x extinction coefficient (k) is low (< 0.05), the most impacting adjustable parameter on the resonant frequency is the real part of the refraction index (n) since it affects the capacitance. For all simulations of Wafer C-11-34 regions, n was initially set to 1.9 [11, 19, 20]. By comparing the experimental peak to the initial simulated peak, the actual value the index could be determined by using the convenient linear relationship given by

36

$$n_2 = n_1 \times \frac{f_1}{f_2} \qquad (12)$$

where n_1 is the initial COMSOL refraction index (1.9), f_1 is the initial COMSOL peak frequency, and f_2 is the experimental data peak frequency. The linear dependence of frequency with refractive index is expected since based on Equation (12), the resonant frequency is inversely proportional to the capacitance, which depends on the square of the refraction index (since $\varepsilon \sim n^2$). The n in the region of interest (3-8 THz) goes up nearly linear fashion as frequency increases, as can be seen with the linear fit in Figure 27. The straight line in Figure 27 is given by

$$n = 1.714 + 0.0602(f), 3THz < f < 8THz \qquad (13)$$

Figure 27.   Refraction Index (Real Portion) vs. Frequency for C-11-34
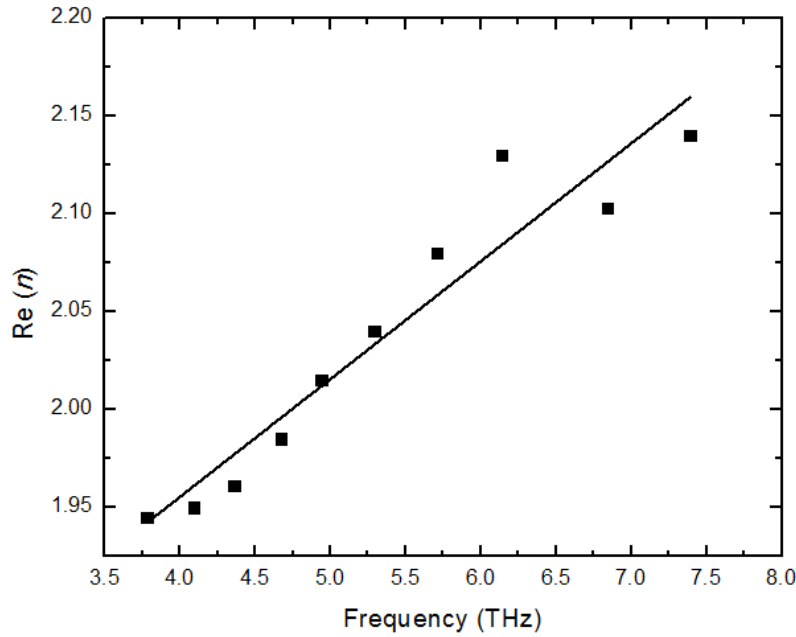
Since frequency varied with square size for Wafer C-11-34, COMSOL was able to be utilized to determine the real part of the refraction index by comparing the experimental data to the initial COMSOL simulations. Initial COMSOL simulations were adjusted accordingly through adjusting the dielectric's real value to match the peak frequency of the experimental data. This lead to a relatively linear data set for Re (n) vs frequency, as shown above and given by the equation: $n = 1.714 + 0.0602$ (f), 3 THz $< f < 8$ THz.

A comparison of simulated absorption spectra using both the initial and corrected values of *n,* along with the experimental (actual) measurement for 15 µm square size metamaterial, is shown in Figure 28. As expected, the peak frequency of the experimental result matches well with the simulated measurement using the corrected index of refraction.

Figure 28.   Example of the Refraction Index Adjustment Between Simulation and Experimental Data
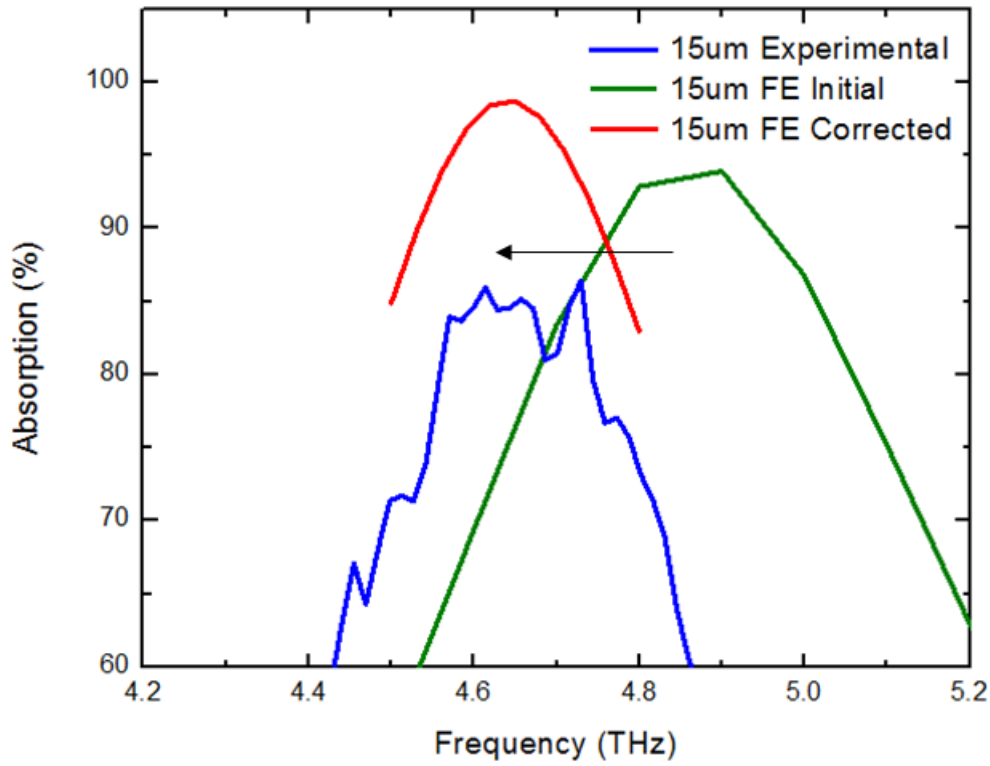
A visual depiction demonstrating how the actual value of the refraction index (*n*) was determined for the 15 µm metamaterial. The black arrow represents the shift of the COMSOL FE simulation from the initial value of *n* of 1.9 (green curve) to the corrected value of 1.985 (red curve). The peak frequency of the red curve matches well with the experimental data (blue curve). This process was used for each metamaterial to determine the variation of *n* with frequency to establish Equation 13.

38

b.   *Resonant Circuit Model*

The experimental data was compared to a theoretical model equating the behavior of a metamaterial to an LRC circuit with R being total resistance, L total inductance, and C total capacitance [11]. For this model, the equivalent circuit is composed of a capacitor in parallel with a resistor and inductor in series. According to the model, the full width half maximum (FWHM) was $2\Gamma = 2(v + \gamma)$, where $v = R/2L$, $\gamma = \beta^2/2CZ_o$, and resonant frequency was $\omega_o = 1/\sqrt{LC}$ [11]. $Z_o = 377 \; \Omega$, and is the impedance of the free space. Because there is assumed zero transmission through the metamaterial, the impedance boundary condition was established, allowing the absorption spectrum of a metamaterial to be given by

$$A = 1 - R = \frac{4v\gamma}{(\omega_o - \omega)^2 + (v + \gamma)^2} \qquad (14)$$

At resonance, $\omega = \omega_o$, and the maximum absorption is given by $A_{max} = 4v\gamma/\Gamma^2$. Equation (14) can then be rewritten as:

$$A(\omega) = \frac{A_{max} \times \Gamma^2}{(\omega_o - \omega)^2 + \Gamma^2} \qquad (15)$$

Using the peak absorption, FWHM, and resonant frequency from the experimental data, it is possible to plot a theoretical absorption spectrum using Equation 15. Figure 29 shows a comparison between the theoretical plot and experimental data for the metamaterial with 18 μm square size. While this does not give explicit values of L, R, and C, it is interesting to note that the experimental data agrees well with the Lorentzian line shape predicted in the circuit model [11].

Figure 29.   Resonant Circuit Model vs. Experimental Data
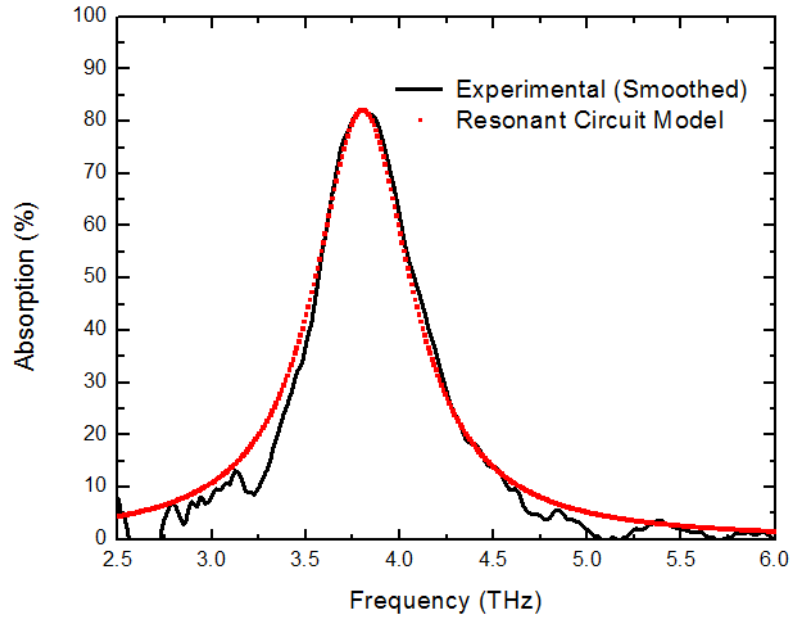
The black curve represents the experimental data of 18 µm square metamaterial, while the red-dotted curve represents the plot using Equation 15. Notice that the experimental data confirms the Lorentzian line shape predicted by the LRC model. Source [11] A. Sellier et al., "Resonant circuit model for efficient metamaterial absorber," *Opt. Soc. of Amer.*, vol. 21, no. S4, pp. A997-A1006, Oct. 2013.

B.   CONSTANT SQUARE SIZE, VARYING PITCH SIZE METAMATERIAL

The second metamaterial configuration discussed has a constant square size (12 µm), with a variable pitch, designated in this text as C-11-31. The pitch sizes ranged from 14 µm to 29 µm, in increments of 3 µm, and 29 µm to 53 µm in increments of 6 µm.

1.   General Observation of C-11-31

The measured absorption spectra for the metamaterials in C-11-31 are shown in Figure 30. General observation shows several interesting characteristics for this set of metamaterials as well with respect to peak frequencies, absorption values, and resonant modes.

Figure 30.   Absorption vs. Frequency for Constant Pitch, Varying Square Size
Metamaterial (C-11-31)
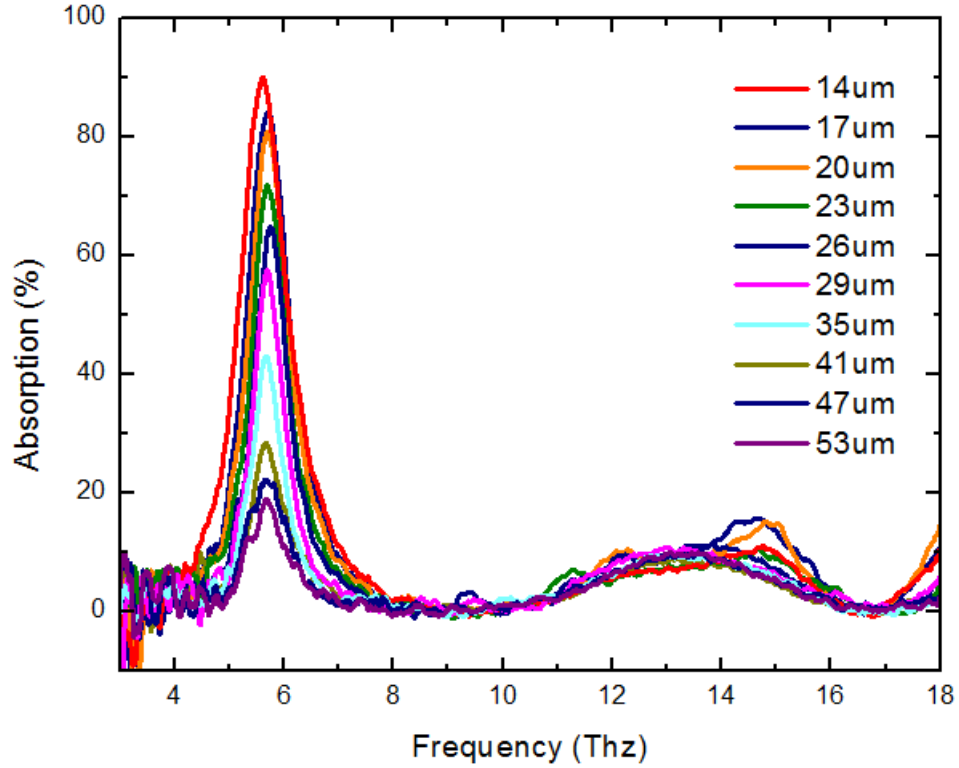
The experimental absorption spectra for wafer C-11-31, with the pitch ranging from 14 µm to 53 µm as denoted in the legend. The square size (12 µm) was held constant for each region. As the pitch increases, there is a mostly steady decrease in peak absorption, while peak frequency is relatively constant. Although this research is primarily focused on the primary mode between 3-8 THz, note the other modes from 10-18 THz with lower absorption peaks.

2.   Absorption Characteristics of C-11-31

Peak frequency stayed relatively constant for all metamaterials in C-11-31. As discussed earlier, resonant frequency is inversely proportional to resonator square size, so it would be expected that resonant frequency remains nearly constant. The resonance peak frequency with respect to fill factor is shown in Figure 31, confirming this behavior. An interesting phenomena, though, is the slight non-linear shift in peak resonant frequency from the 14 µm to 26 µm pitch metamaterials. This can be viewed with clarity in Figure 32. While the exact mechanism for this result is unknown, it should be noted that as the fill factor decreases, the resonant frequency is much more consistent. This

suggests that the effect of coupling between adjacent cells plays a factor in the resonant frequency variations when the gap between the adjacent squares is smaller. For this research, it appeared that a gap around 14 μm was the point at which coupling was minimized.

Figure 31.   C-11-31 Peak Frequency vs. Fill Factor
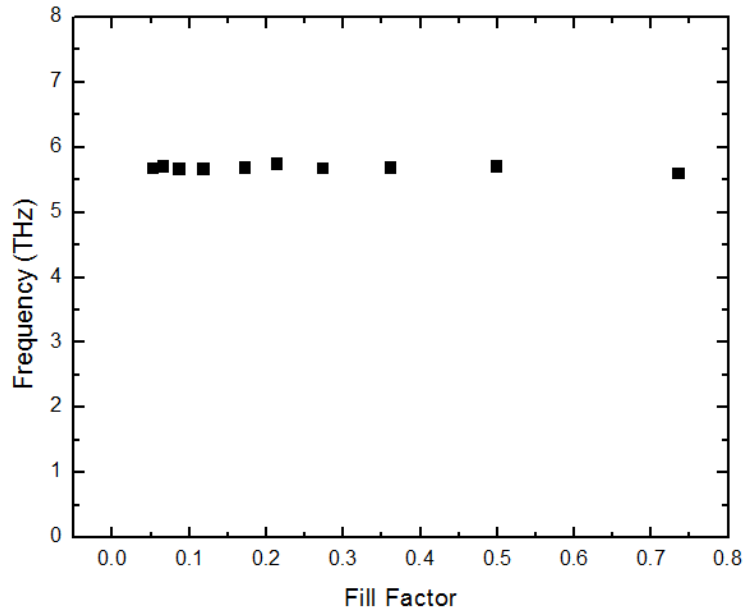
The frequency was relatively constant for C-11-31 as was expected for a resonator with a constant square size.

Figure 32.   C-11-31 Absorption vs. Frequency for the Main Mode
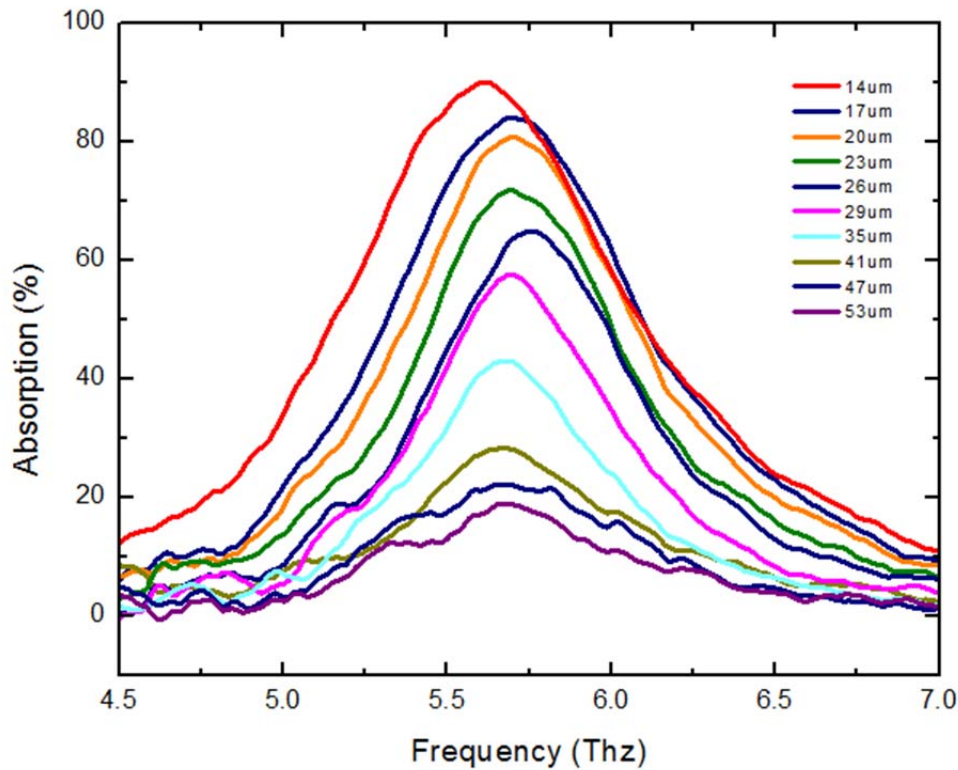
The main mode absorption vs frequency characteristics for Wafer C-11-31. Note the slight non-linear shift in peak frequency from the 14 μm - 26 μm pitch. From 29 μm - 53 μm the resonant frequency was relatively constant.

Maximum absorption occurred for the metamaterial with the highest fill factor, similar to the results for Wafer C-11-34. As the gap goes up, and hence fill factor, goes down, absorption magnitude goes down as well. The relationship for absorption magnitude with fill factor and gap is shown in Figure 33. It should be noted that C-11-31 had a much wider range of fill factors, making it difficult to compare the metamaterials of both wafers against each other. Figure 34 shows an overlap of the absorption peak vs. gap size for both C-11-31 and C-11-34. While they do not align completely, there is a consistent trend between the two samples.

Figure 33.   C-11-31 Peak Absorption vs. Fill Factor and Gap (μm)
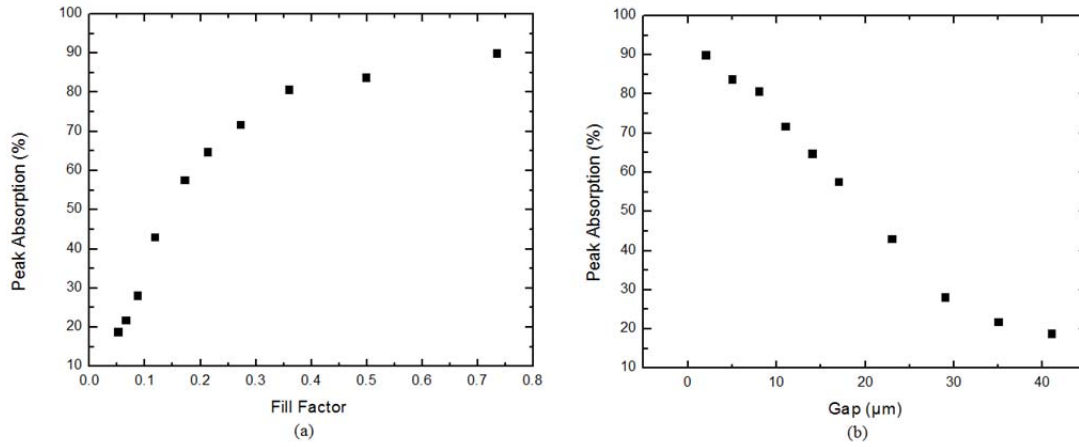
Fill factor (a) is the dimensionless ratio of the area of the resonator vs the area of the unit cell, while gap (b) is the distance between each unit cell. A larger fill factor leads to higher peak absorption. Conversely, a larger gap, and thus a smaller fill factor, leads smaller peak absorption.

Figure 34.   Peak Absorption vs. Gap for C-11-34 and C-11-31
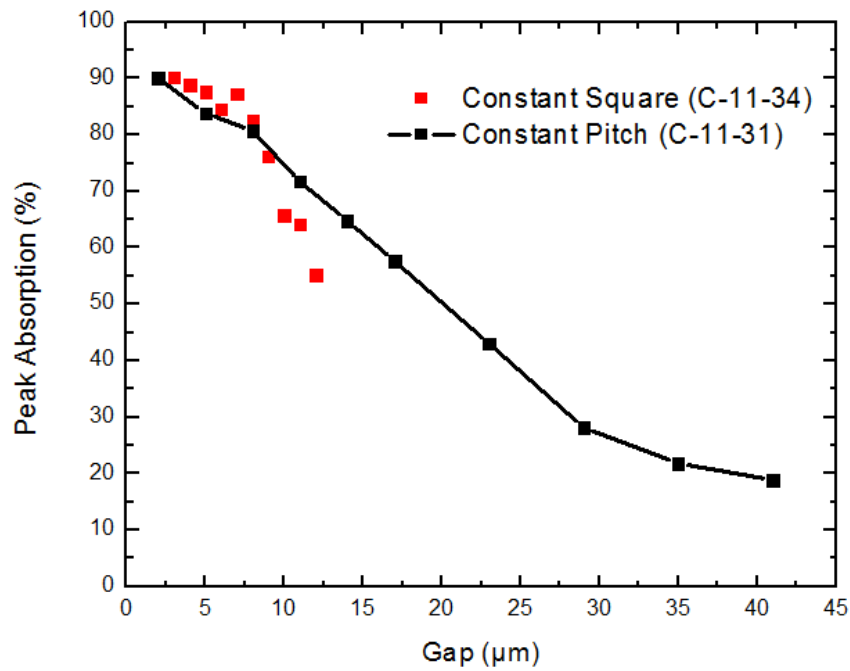
Both wafers had mostly consistent results with respect to the gap size and the peak absorption.

VI.   CONCLUSION

This research began by utilizing COMSOL FE simulations to investigate the absorption characteristics of $Al/SiO_x/Al$ metamaterial absorbers with a main mode resonance between 3–8 THz. Two configurations were studied, one with a constant pitch and variable resonator square size, the other with a constant resonator square size and variable pitch. Once the FE simulations provided a baseline for the desired unit cell geometry, several trials were conducted for the photolithography, development, and etching processes utilizing the microfabrication devices in the NPS clean room. Process times were established through these trials and were utilized in the final fabrication of a constant pitch, variable square size metamaterial. The fabrication of this metamaterial marked the first time the entire etching process was completed in the NPS clean room for an $Al/SiO_x/Al$ metamaterial absorber. After fabrication, FTIR testing was employed to determine the absorption characteristics for each metamaterial configuration. Analysis of the FTIR testing revealed several modes of absorption for each metamaterial, although this research was focused on the main mode. Interestingly, the experimental data matched with a previously developed theoretical resonant circuit model and demonstrated the linear relationship between a metamaterial's refraction index and its resonant frequency [11].

The results provide groundwork for the SRL to fabricate an uncooled bi-material sensor using metamaterial resonant absorbers. Ideally, a bi-material thermal device can be maximized using the analysis from the two metamaterial configurations investigated during this research. Ultimately, simplifications in the fabrication process, along with less expensive, more prevalent THz radiation sources, can make THz sensors widespread for a wide variety of naval security and imaging processes.

THIS PAGE INTENTIONALLY LEFT BLANK

APPENDIX. ADDITIONAL FABRICATION DATA

A. TEST RUN DATA

Table 5.   Pre-Fabrication Test Run # 1

Mask Unit Cell Size (μm)	Actual Unit Cell Size
18	18.7
17	17.5
16	16.5
15	15.3
14	14.3
13	13.5
12	12.3
11	11.1
10	10.3
9	9.2

Light Integra Setting 100, Print Gap 40 μm, Align Gap 50 μm, and Development Time 60 seconds.

Table 6.   Pre-Fabrication Test Run # 2

Mask Unit Cell Size (μm)	Actual Unit Cell Size
18	18.3
17	17.1
16	16.2
15	15.3
14	14.9
13	13.9
12	12.5
11	11.8
10	10.5
9	9.0

Light Integra Setting 105, Print Gap 40 μm, Align Gap 50 μm, and Development Time 60 seconds.

Table 7.   Pre- Fabrication Test Run # 3

Mask Unit Cell Size (µm)	Actual Unit Cell Size
18	18.5
17	17.6
16	16.5
15	15.7
14	15.1
13	14.0
12	13.0
11	11.9
10	10.9
9	10.2

Light Integra Setting 110, Print Gap 10 µm, Align Gap 50 µm, and Development Time 60 seconds.

Table 8.   Pre-Fabrication Test Run # 4

Mask Unit Cell Size (µm)	Actual Unit Cell Size
18	18.3
17	17.7
16	16.5
15	15.7
14	15.1
13	14.1
12	12.7
11	11.6
10	10.8
9	9.6

Light Integra Setting 115, Print Gap 10 µm, Align Gap 50 µm, and Development Time 60 seconds.

Table 9.   Pre-Fabrication Test Run # 5

Mask Unit Cell Size (µm)	Actual Unit Cell Size
18	18.0
17	17.1
16	16.3
15	15.5
14	14.3
13	13.3
12	12.1
11	11.3
10	10.3
9	9.2

Light Integra Setting 120, Print Gap 10 µm, Align Gap 50 µm, and Development Time 60 seconds.
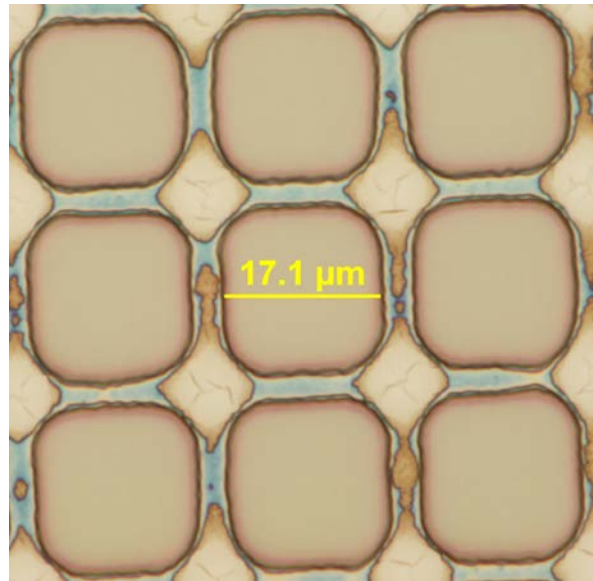
B.   TEST RUN IMAGES

Figure 35.   Pre-Fabrication Test Run #1, Wafer C-11-34, 17 µm Square
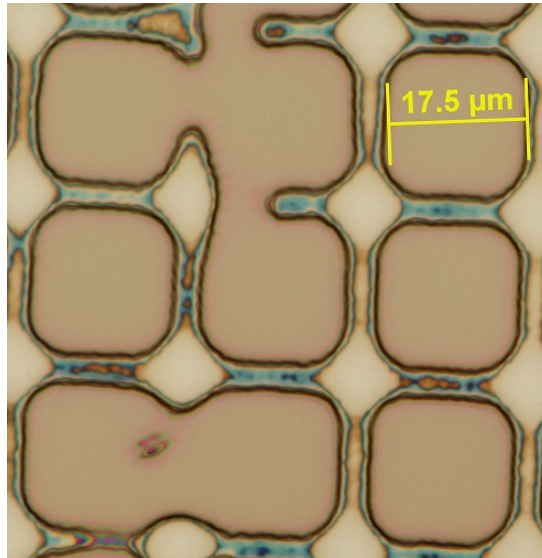
Notice that several resonators are interconnected due to an exposure time that was too short. The light blue color surrounding the resonators is caused by light diffraction from too large a print gap.

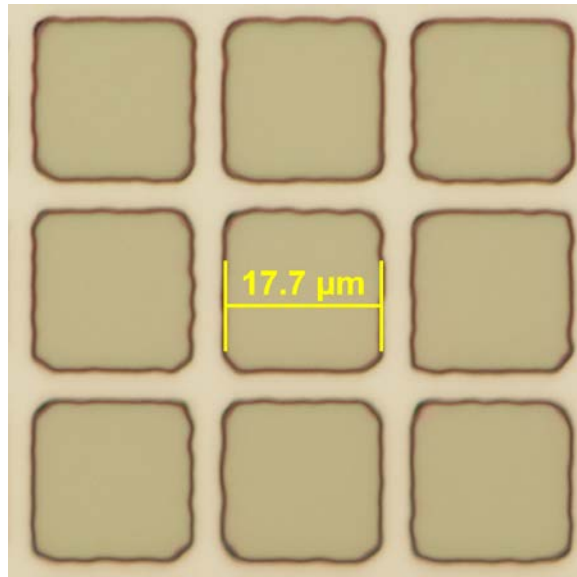Figure 36.   Pre-Fabrication Test Run # 2, Wafer C-11-34, 17 µm Square

With a slightly longer exposure time, Test Run #2 did not have any connected resonators, but the large print gap created a significant diffraction pattern around the resonator.

Figure 37.   Pre-Fabrication Test Run # 3, Wafer C-11-34, 17 µm Square
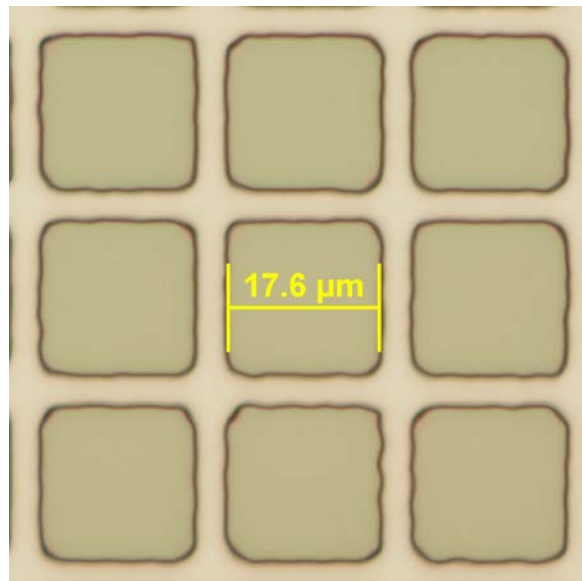
A reduced print gap to 10 µm from 40µm eliminated diffraction, yet the resonators were clearly distorted and larger than expected. The exact reason for the waviness of the resonator outer edges was not determined, but could have resulted from an unclean mask.

Figure 38.   Pre-Fabrication Test Run # 4, Wafer C-11-34, 17 µm Square

Test Run #4 increased the exposure time from the previous test run with no improvement.
The mask was cleaned with acetone and isopropyl after this test run.

Figure 39.   Pre-Fabrication Test Run # 5, Wafer C-11-34, 17 µm Square
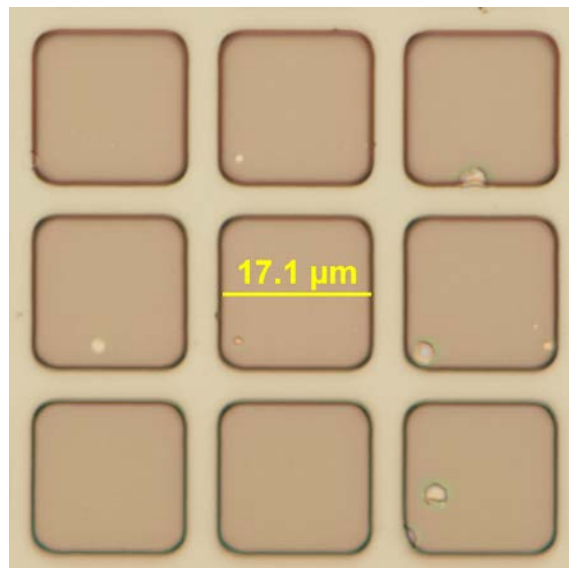
Test run #5 produced a resonator with its size within 0.1µm of the mask size. Notice that
the resonator edges are also much smoother from previous test runs. The small
perfections resulted from the mask having small residue from the acetone and isopropyl
wash. This effect was successfully eliminated during the fabrication of Wafer C-11-34.

Figure 40.   Fabrication of C-11-34, 18 µm Square
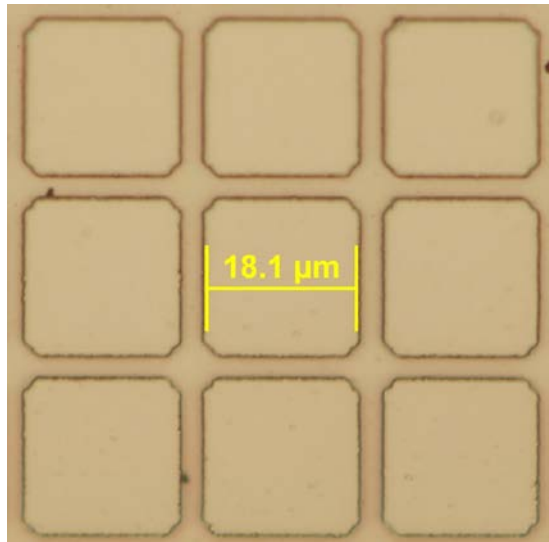
Note the well-defined resonator features for Wafer C-11-34, as compared to the test runs. The dimension of the resonator, 18.1 µm, is very close to the measured mask square size of 18.0 µm

LIST OF REFERENCES

[1]   C. Sirtori, "Bridge for the terahertz gap," *Nature,* vol. 417, pp. 132–133, May 2014.

[2]   J. F. Federici et al., "THz imaging and sensing for security applications—explosives, weapons, and drugs," *Semicond. Sci. Technol.*, vol. 20, no. 7, pp. S266–S280, 2005.

[3]   Z. D. Taylor et al., "Reflective terahertz imaging of porcine skin burns," *Opt. Lett.*, vol. 33, no. 11, pp. 1258–1260, May 2008.

[4]   J.E. Bjarnason et al., "Millimeter-wave, terahertz, and mid-infrared transmission through common clothing," *Appl. Phys. Lett.*, vol. 85, no. 4, pp. 519–521, July 2004.

[5]   Q. Mao et al., "High-speed and broadband terahertz wave modulators based on large-area graphene field effect transistors," *Opt. Lett.*, vol. 39, no. 19, pp. 5649–5652, Sep. 2014.

[6]   CIRCE. (n.d.). "Filling the THz Gap" [Online]. Available: http://circe.lbl.gov/THzGap.html. Accessed Oct. 29, 2015.

[7]   F. Alves et al., "Bi-material terahertz sensors using metamaterial structures." *Opt. Expr.*, vol. 20, no. 11, pp. 13256–13271, May 2013.

[8]   A. A. Gowen et al., "Terahertz time domain spectroscopy and imaging: emerging techniques for food process monitoring and quality control," *Trends Food Sci. Technol.*, vol. 25, no. 1, pp. 40–46, 2012.

[9]   S. M. Kim et al., "Biomedical terahertz imaging with a quantum cascade laser," *Appl. Phys. Lett.*, vol. 88, no. 15, p. 153903, 2006.

[10]   N.M. Burford et al., "Terahertz imaging for nondestructive evaluation of packaged power electronic devices," *Intl. Journ. of Emerging. Tech. and Adv, Eng.*, vol. 4, no. 1, pp. 395–401, Jan. 2014.

[11]   A. Sellier et al., "Resonant circuit model for efficient metamaterial absorber," *Opt. Soc. of Amer.*, vol. 21, no. S4, pp. A997-A1006, Oct. 2013.

[12]   Q.-Y Wen et al., "Transmission line model and fields analysis of metamaterial absorber in the terahertz band," *Opt. Expr.*, vol. 17, no. 22, pp. 20256–20265, Oct. 2009.

[13]   L. Piazza et al., "Simultaneous observation of the quantization and interference pattern of a plasmonic near-field," *Nat. Comms.*, vol. 6, no. 6407, pp. 1–7, Mar. 2015.

[14]   L. Huang et al., "Experimental demonstration of terahertz metamaterial absorbers with a broad and flat high absorption band," *Opt. Lett,* vol. 37, no. 2, pp. 154–156, 2012.

[15]   N. I. Landy et al., "A perfect metamaterial absorber," *Phys. Rev. Lett,* vol. 100, no. 20, pp. 207402-1 -207402-4 May 2008.

[16]   B. Kearney et al., "Al/SiO$_x$/Al single and multiband metamaterial absorbers for terahertz sensor applications," *Opt. Eng.*, vol. 52, no. 1, pp. 013801-8–013801-2, 2013.

[17]   B.T. Kearney, "Enhancing microbolometer performance at terahertz frequencies with metamaterial absorbers," Ph.D. dissertation, Appl. Phys. Dept., Naval Postgraduate School, Monterey, CA, Sep. 2013.

[18]   A.T. Phillips, "Resonant terahertz absorption using metamaterial structures," M.S. thesis, Appl. Phys. Dept., Naval Postgraduate School, Monterey, CA, Dec. 2012.

[19]   R. Kitamura et al., "Optical constants of silica glass from extreme ultraviolet to far infrared at near room temperature," *App. Opt.*, vol. 46, no. 33, pp. 8118–8133, Nov. 2007.

[20]   M. K. Gunde and M. Macek, "Infrared optical constants and dielectric response functions of silicon nitride and oxynitride films," *Phys. Status Solidi*, vol. 183 A, no. 2, pp. 439–449, 2001.

[21]   Fabio Alves, private communication, July 2015.

[22]   Kirt Blattenberger, 2015, *Skin Depth Calculator,* [Online].Available: http://www.rfcafe.com/references/calculators/skin-depth-calculator.htm

[23]   Andrew Strikwerda, private communication, July 2015.

[24]   H.-T. Chen, "Interference theory of metamaterial perfect absorbers," *Opt. Expr.*, vol. 20, no. 7, pp. 7165–7172, Mar. 2012.

INITIAL DISTRIBUTION LIST

1.   Defense Technical Information Center
        Ft. Belvoir, Virginia

2.   Dudley Knox Library
        Naval Postgraduate School
        Monterey, California